Journal Pre-proof

Influence of scandium addition on the castability, elevated-temperature tensile and fatigue performance of A356 alloy

Priyansh Khandelwal, Raluca Florentina Negrea, Asad Hayat, Jason Nunn, Scott Honan, Shouxun Ji



PII: S0925-8388(26)06537-0

DOI: https://doi.org/10.1016/j.jallcom.2026.192467

Reference: JALCOM192467

To appear in: *Journal of Alloys and Compounds*

Received date: 28 August 2026
Revised date: 9 November 2026
Accepted date: 13 November 2026

Please cite this article as: Priyansh Khandelwal, Raluca Florentina Negrea, Asad Hayat, Jason Nunn, Scott Honan and Shouxun Ji, Influence of scandium addition on the castability, elevated-temperature tensile and fatigue performance of A356 alloy, *Journal of Alloys and Compounds,* (2026) doi:https://doi.org/10.1016/j.jallcom.2026.192467

This is a PDF of an article that has undergone enhancements after acceptance, such as the addition of a cover page and metadata, and formatting for readability. This version will undergo additional copyediting, typesetting and review before it is published in its final form. As such, this version is no longer the Accepted Manuscript, but it is not yet the definitive Version of Record; we are providing this early version to give early visibility of the article. Please note that Elsevier's sharing policy for the Published Journal Article applies to this version, see: https://www.elsevier.com/about/policies-and-standards/sharing#4-published-journal-article. Please also note that, during the production process, errors may be discovered which could affect the content, and all legal disclaimers that apply to the journal pertain.

© 2026 Published by Elsevier.

Journal Pre-proof

Influence of scandium addition on the castability, elevated-temperature tensile and fatigue performance of A356 alloy

Priyansh Khandelwal[a], Raluca Florentina Negrea[a], Asad Hayat[a], Jason Nunn[b], Scott Honan[c], Shouxun Ji[a*]

[a] Brunel Centre for Advanced Solidification Technology (BCAST), Brunel University London, Uxbridge UB8 3PH, United Kingdom

[b] NioCorp Technologies Limited, 3rd Floor 86 - 90 Paul Street, London, England, EC2A 4N

[c] NioCorp Developments Ltd., 7000 South Yosemite, Suite 115, Centennial, CO, 80122, USA

*Corresponding authors: Shouxun.Ji@brunel.ac.uk

Abstract

The influence of scandium (Sc) addition on the fluidity, grain-refinement fading, elevated-temperature tensile performance and fatigue behaviour of A356.2 alloy was systematically investigated. The addition of 0.2 wt.% Sc increased fluidity by 19.5% compared with the baseline alloy, whereas higher Sc additions reduced fluidity because of coarse primary Sc-containing intermetallics. Sc addition significantly refined the grain structure, reduced the secondary dendrite arm spacing (SDAS), modified the eutectic Si morphology and transformed Fe-containing intermetallic phases, resulting in a less heterogeneous microstructure. The Sc-modified alloy also exhibited relatively stable grain size during prolonged melt holding under the present experimental conditions, with only a 14% increase in grain size after 240 min of melt holding. Following T6 heat treatment, the Sc-modified alloy exhibited higher tensile strength and ductility at 200 °C. Atomic-resolution HAADF-STEM and STEM-EDS analyses confirmed ordered $AlSc_2Si_2$ dispersoids and revealed their close spatial association with Mg-Si-based precipitates and localised Mg enrichment at the dispersoid/α-Al interface. Crystallographic analysis further identified U1-$(Al,Si)_2Mg$ at the examined interface, suggesting that this interfacial configuration may modify the local Mg-Si precipitation environment and contribute to strength retention during elevated-temperature deformation. The A356-0.2Sc-T6 alloy exhibited higher fatigue lives at several investigated stress amplitudes, although the response was not consistently improved across the entire stress range. The results demonstrate that Sc addition can modify the castability, microstructure and mechanical response of A356 alloy under the investigated conditions.

Key words: A356 alloy; Fluidity; Fading; Fatigue behaviour; Scandium; High-temperature Tensile Test

.

Journal Pre-proof

1. Introduction

Al-Si-Mg casting alloys, particularly A356.2 (Al-7Si-0.3Mg), are widely used in automotive and aerospace structural components due to their excellent castability, good strength-to-weight ratio, corrosion resistance and good response to heat treatment. However, rising service demands, such as higher operating temperatures, cyclic loading conditions, and lightweight design specifications, require improvements in the fatigue resistance and thermal stability of this alloy without compromising casting performance [1–3].

Microalloying with scandium (Sc) has emerged as a highly effective approach to overcome these limitations by simultaneously modifying solidification behaviour and precipitation kinetics. Sc additions promote grain refinement by forming stable heterogeneous nucleation particles during solidification and contribute to precipitation strengthening through thermally stable Sc-containing particles after heat treatment. Previous studies on Sc-modified A356.2 alloys have demonstrated that Sc can simultaneously refine primary α-Al grains, modify the morphology of eutectic Si and alter Fe-bearing intermetallic phases, resulting in significant improvements in strength and ductility under both as-cast and heat-treated conditions. Recent work by the authors [4,5] established an optimum Sc addition range of 0.2-0.4 wt.% in A356 alloys, where a balance between microstructural refinement and mechanical performance is achieved, whereas higher Sc additions were found to promote the formation of coarse Al-Si-Sc intermetallics that degrade the mechanical properties.

Despite these advantages, the broader application of Sc-modified A356.2 alloys is constrained by an incomplete understanding of their processing-microstructure-property relationships, particularly in casting conditions. One critical concern is the potential deterioration of castability with increasing Sc content. The addition of Sc alters the solidification path by shifting liquidus and eutectic temperatures and promoting the formation of primary and secondary Sc-containing intermetallic phases. These changes influence the evolution of the solid fraction during solidification, dendrite coherency, and feeding behaviour, which collectively govern melt flow characteristics. Fluidity, defined as the maximum distance a liquid metal can flow before solidification, is therefore highly sensitive to Sc-induced microstructural evolution and plays a decisive role in defect formation in thin-section or complex castings [6]. However, the influence of Sc-induced solidification behaviour on the fluidity of A356.2 alloys remains poorly understood.

Another important processing challenge is the stability of grain refinement during melt holding. Conventional grain refiners such as Al-Ti-B suffer from fading, which refers to the progressive loss of nucleation potency due to dissolution of $TiAl_3$ particles, agglomeration or sedimentation of TiB_2, and solute interactions that reduce nucleation effectiveness. This results in coarser grains, increased dendrite arm spacing, higher undercooling and deterioration in mechanical properties, often within short holding times of 20-30 minutes [7–10]. This sensitivity to processing time presents a significant limitation in industrial casting operations, where melt holding and transfer are often unavoidable. In this context, Sc can be used as a promising alternative grain refiner due to the formation of a thermodynamically stable $Al_3Sc/(Al, Si)_3(Sc, Ti)$ phase, which exhibits high resistance to dissolution and coarsening at elevated temperatures. These characteristics suggest that Sc may offer greater resistance to fading compared to conventional refiners. Nevertheless, systematic studies correlating melt holding time with the evolution of grain structure, solidification behaviour, and resulting mechanical properties in Sc-modified A356.2 alloys remain limited.

In addition to castability, the mechanical properties of A356.2 alloys under elevated-temperature conditions is of interest for alloy development, particularly because the strengthening contribution of Mg_2Si precipitates formed during T6 heat treatment can deteriorate with increasing temperature. Although A356.2 is widely used in transportation and automotive castings, alloys intended for more demanding elevated-temperature applications may use additional alloying elements to improve the stability of strengthening phases and mechanical properties at elevated temperatures. The addition of Sc can promote the formation of Sc-containing Al-Si phases, which may influence the precipitation microstructure and consequently the mechanical properties at elevated temperature. While the role of Sc in improving room-temperature properties and microstructural refinement has been investigated extensively, its influence on the elevated-temperature tensile behaviour of cast A356.2 remains insufficiently explored. Therefore, the present study evaluates the tensile response of Sc-modified A356.2 at 200 °C to assess the potential of Sc as a microalloying addition for improving elevated-temperature mechanical performance.

Fatigue performance is another critical factor governing the reliability of cast aluminium components. In conventional A356.2 alloys, fatigue crack initiation is typically associated with microstructural heterogeneities such as coarse eutectic Si, Fe-rich intermetallics, and casting defects such as oxides, porosity, and inclusions [1]. Grain refinement and

microstructural homogenisation can reduce the effective size of crack initiation sites and delay crack nucleation, while stable dispersoids may influence crack propagation behaviour. Although Sc additions are expected to improve fatigue resistance through these mechanisms, comprehensive studies linking Sc-induced microstructural evolution to fatigue crack initiation and growth behaviour in A356.2 alloys are still scarce.

From an industrial application perspective, the combination of these properties is particularly relevant to cast aluminium components used in automotive engine applications, such as cylinder heads. During manufacturing, the molten alloy may undergo holding periods before casting, making the stability of grain refinement an important consideration for maintaining consistent casting quality. In service, components such as cylinder heads are exposed to elevated temperatures and repeated mechanical and thermal loading, requiring adequate high-temperature strength and fatigue resistance. Therefore, investigating the fading behaviour, elevated-temperature tensile properties and fatigue performance together provides a more comprehensive assessment of the potential of Sc-modified A356.2 alloys for demanding casting and automotive applications.

Previous studies by the authors [4,5] have established the effects of Sc addition on the solidification behaviour, microstructure and room-temperature mechanical properties of A356.2 alloys and identified an optimum Sc addition range. However, these studies primarily focused on alloy design, microstructural evolution and conventional mechanical properties. The effects of Sc addition on casting fluidity, the retention of grain-refining effectiveness during prolonged melt holding, elevated-temperature tensile behaviour and fatigue performance have not been systematically evaluated within the same alloy system. In particular, the relationship between Sc-induced microstructural refinement and melt-holding stability, together with the role of Sc-containing phases in elevated-temperature and fatigue behaviour, remains insufficiently established.

Therefore, the present study extends the previous work by systematically investigating the influence of Sc addition on fluidity, grain-refinement stability during prolonged melt holding, elevated-temperature tensile behaviour and fatigue performance of A356.2 alloy. Microstructural, phase and atomic-scale characterisation are further combined with CALPHAD analysis to relate the observed processing and mechanical responses to the evolution of Sc-containing phases. The objectives are to: (i) evaluate the influence of Sc

addition on fluidity in relation to solidification behaviour, (ii) assess the stability of Sc-induced grain refinement during prolonged melt holding and its relationship with mechanical properties, (iii) evaluate tensile behaviour at 200 °C, and (iv) investigate fatigue performance and fracture characteristics in relation to the evolved microstructure.

2. Materials and Methods

2.1 Alloy Design- Thermodynamic Calculations (CALPHAD)

Thermodynamic simulations for the Al-Si-Mg-Sc system were performed using the CALPHAD approach in Thermo-Calc® 2026a software with the TCAL8 database. The calculations were performed over the temperature range of 200-750 °C using the experimentally measured alloy compositions listed in Table 1 to evaluate the equilibrium phase fractions, predicted solidification sequence and phase stability as a function of Sc content. These calculations were used primarily to identify thermodynamic trends associated with the formation of Sc-containing phases. It should be noted that the calculations represent equilibrium conditions and therefore do not directly reproduce the non-equilibrium solidification and melt-filling behaviour occurring during the spiral fluidity test.

2.2 Alloy Preparation

Commercial A356.2 alloy was used as the baseline material for this study, with the nominal composition shown in Table 1. Three experimental alloys were prepared by adding Sc in the form of an Al-2 wt.% Sc master alloy to achieve target compositions of 0.2, 0.4 and 0.6 wt.% Sc, in addition to the baseline A356.2 alloy. The alloys were melted in an electric resistance furnace using a graphite-SiC crucible at 760 °C. The A356.2 alloy and Al-20 wt.% Si master alloy were first added to the crucible and melted together. The Al-2 wt.% Sc master alloy was then added and the melt was allowed to homogenise for 1 h, with intermittent stirring during this period. Approximately 15 min before degassing, Al-25 wt.% Mg master alloy was added and. The melt temperature was monitored using a K-type thermocouple. The Al-20Si and Al-25Mg additions were controlled to compensate for dilution and achieve the target alloy compositions. The melt was covered with a commercial granular flux, then subjected to degassing, during which high-purity argon was blown into the melt using a rotary degasser at 300 rpm and a gas flow rate of 6 l/min for 6-8 min. Dross was skimmed, and the melt was held until it reached 725 °C. Hydrogen porosity and melt cleanliness were assessed using the Reduced Pressure Test (RPT) to get the Density Index (DI), which was measured on the

IDECO hydrogen analyser using double sample crucibles under vacuum and atmospheric pressure. Simultaneously, cooling curve analysis was done on the IDECO thermal analysis system by placing a thermocouple in the centre of a cylindrical sample cup. It was ensured that the DI was less than 1 %. Thereafter, the melt was poured at 720 ± 5 °C in BS L101 permanent steel moulds pre-heated at 200 °C to obtain cylindrical samples of 20 mm diameter and 150 mm length, which were then machined to get tensile and fatigue test samples as shown in Figure 1. The mould temperature was measured consistently with a contact thermocouple to ensure similar cooling rates across all alloys. The A356 and A356-0.2Sc samples were solution treated at 540 °C for 8 hours, followed by immediate water quenching to room temperature, while the A356-0.4Sc alloy samples were solution treated at 535°C for 7h. Artificial ageing for all alloys were carried out at 170 °C for 8 hours (T6 condition) [5] .

Table 1 Chemical composition of the experimental A356.2-Sc alloys measured by optical emission spectroscopy (OES), wt.%

Alloy name	**Al**	**Si**	**Mg**	**Fe**	**Sc**	**Ti**
Baseline A356	Bal.	6.96	0.33	0.11	-	0.12
A356-0.2 Sc	Bal.	7.14	0.31	0.10	0.208	0.11
A356-0.4 Sc	Bal.	7.27	0.31	0.09	0.402	0.10
A356-0.6Sc	Bal.	7.34	0.30	0.10	0.607	0.09

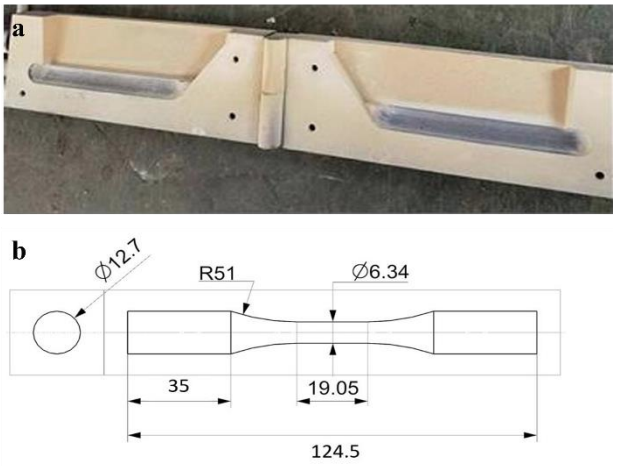


Figure 1 (a) BS L101 permanent steel mould to get the specimen for mechanical testing; and (b) fatigue sample machined from the cylindrical bar obtained from the mould.

2.3 Melt Holding and Fading Behaviour Evaluation

Fading behaviour was evaluated using controlled melt holding experiments designed to simulate industrial holding conditions. Approximately 9 kg of A356-0.4Sc alloy melt was prepared in an electric resistance furnace. This alloy was selected because it exhibited the most refined grain structure among the three Sc-containing variants investigated in our previous study[5], making it representative for evaluating the stability of Sc-induced grain refinement during prolonged melt holding. To minimise oxidation and atmospheric contamination during melt holding, the furnace chamber was maintained under continuous argon shielding. A T-joint connection was attached to the degassing system, through which argon was supplied at 5 l/min throughout the holding period. The shielding arrangement consisted of two steel wire delivery tubes: one positioned near the bottom of the furnace chamber, close to the crucible and the second positioned above the melt surface to provide uniform inert gas coverage. This configuration ensured effective displacement of atmospheric air and minimised oxygen intake into the melt, thereby isolating effects from oxidation-related influences (as shown in Figure 2). Immediately after degassing, the first casting was poured and designated as the 0-min holding condition, and a mushroom mould sample was cast for chemical composition verification using optical emission spectroscopy (OES). Subsequently, the melt was held at 725 ± 5 °C, and additional castings were produced after holding times of 30, 60, 120, 180 and 240 min, resulting in six holding durations in total. At each holding interval, the density index (DI) was measured to assess hydrogen content and melt cleanliness and the cooling curve was analysed using the IDECO thermal analysis system. A TP1 mould casting was produced to ensure a standardised cooling rate of approximately 3.5 K/s for grain-refinement evaluation, and two tensile bars were cast for mechanical testing. The melt was not stirred during the holding time.

Journal Pre-proof



Figure 2 (a) & (c) Overall furnace and gas supply system showing argon cylinder and regulator assembly; (b) T-joint connection integrated with the degassing unit to enable continuous argon supply during melt holding; (d) interior view of the furnace showing dual steel wire gas delivery tubes positioned within the furnace chamber to provide inert atmosphere shielding.

2.4 Fluidity Testing

Fluidity tests were conducted on the baseline A356.2 and all three Sc-modified A356 alloys using the standard spiral mould method under controlled casting conditions, as shown in Figure 3. For each alloy, 6 kg of melt was prepared and degassed for 6 min at 6 L/min with high-purity argon to minimise hydrogen-induced porosity. The measured D.I. before pouring was between 0.3 and 0.5, ensuring high melt cleanliness. Cooling curve analysis was performed before casting, and a mushroom-mould sample was taken for compositional verification. The spiral mould was preheated to 350 ± 10 °C, and the melt was poured at 720 ± 5 °C. A total of seven spiral castings were produced for each alloy to obtain statistically

reliable average fluidity length measurements. The filled spiral length was measured and averaged to determine the fluidity performance.

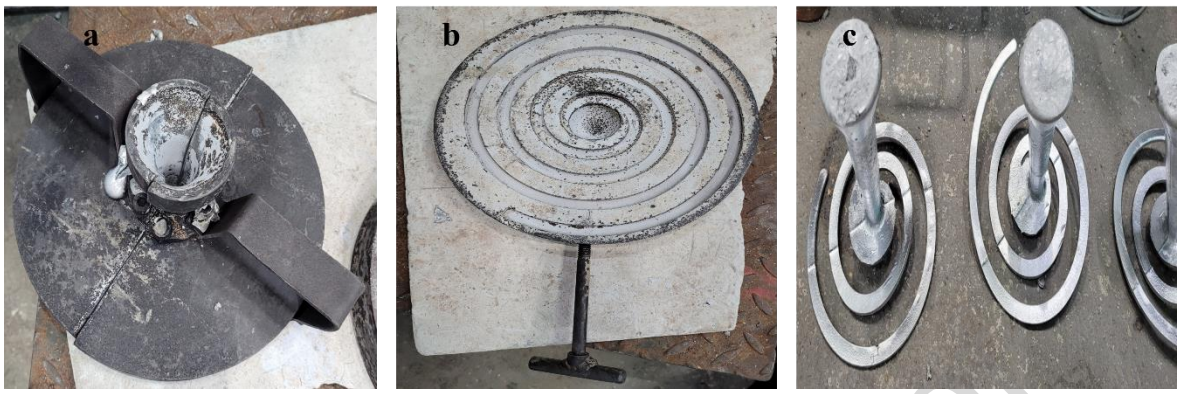


Figure 3 Fluidity test setup and cast samples: (a) top view of the spiral fluidity mould assembly with central pouring basin, (b) spiral channel geometry used to evaluate melt flow characteristics, and (c) solidified castings showing the extent of metal flow along the spiral, used to quantify fluidity length.

2.5 Tensile Testing: Room Temperature and Elevated Temperature

To investigate the effect of melt holding time on the mechanical properties, tensile tests were undertaken at ambient temperature for A356-0.4Sc alloy held up to 240 minutes on an Instron 5892 universal electromechanical testing machine equipped with Bluehill software. For each holding time, two tests were conducted to determine the average tensile properties of the alloy and to correlate the results with the grain-size. High-temperature tensile tests were conducted on T6-treated baseline A356.2, A356-0.2Sc and A356-0.4Sc alloy specimens at 200 °C using a high-temperature furnace attachment on the same universal electromechanical testing machine in accordance with ASTM E21. Three samples were tested per condition and the reported values represent the average of them with standard deviation. For each condition Specimens were held at test temperature for 60 minutes before loading to ensure thermal equilibrium. Testing was performed at a constant strain rate of 1 mm/min, equivalent to room-temperature testing. The yield strength (0.2% offset), ultimate tensile strength (UTS), and elongation to fracture were measured.

2.6 Fatigue Testing

Fatigue specimens were machined from T6-treated cast bars in accordance with ASTM E466-21 as shown in Figure 1b. After machining, all specimens were polished using 2500-grit SiC paper to obtain a uniform surface finish. Surface roughness measurements were performed

using a Mitutoyo SJ-210 surface roughness unit to ensure that surface condition did not influence fatigue performance. The measurements were taken within the gauge length of the sample. Five readings were taken for each sample to obtain the average surface roughness values (R_a). Fatigue tests were conducted using an Instron 8801 servo-hydraulic fatigue testing machine at room temperature. Constant-amplitude loading was applied at stress levels ranging from 75 MPa to 175 MPa. Testing was performed at 15 Hz with a stress ratio R = -1. A single fatigue specimen was tested at each stress amplitude for each alloy condition. This experimental design was adopted to characterise the S-N response over a relatively broad range of stress amplitudes using specimens produced from the same casting batch as the other mechanical tests. In cast Al alloys, fatigue life can exhibit substantial scatter because of casting-related defects and local microstructural heterogeneity. Therefore, rather than using replicate specimens at a limited number of stress amplitudes and reporting averaged fatigue lives, the available fatigue specimens were distributed across a larger number of stress amplitudes to capture the stress-dependent fatigue response. The use of specimens from the same casting batch also minimised additional variation associated with differences in alloy composition and casting conditions.

2.7 Microstructure and Phase Characterisation

For grain-size measurement, the TP-1 sample was sectioned 38 mm above the base, corresponding to the standard evaluation plane. The cooling rate in this section was approximately 3.5 °C/s, providing a reproducible and controlled solidification condition for grain-size comparison. The sectioned samples were ground and polished following standard metallographic procedures. Grain boundaries were revealed using electrochemical anodising (Barker's reagent: 200 mL H_2O + 10 mL 35% HBF_4) under polarised light microscopy. Anodization was performed at 10 V for 45-50 s to produce colour contrast between grains. Quantitative analysis of the microstructure, including grain size and porosity related measurements were done via ImageJ software. At least five fields were analysed per sample to ensure statistical reliability. Fracture surfaces were examined using a Crossbeam 340 FEG SEM-FIB operating at 15 kV to identify crack initiation sites, crack propagation characteristics and failure mechanisms. Transmission Electron Microscopy (TEM) was carried out using ThermoFisher Spectra 300 operated at 200 kV for structural characterisation of particles and precipitates down to atomic level. TEM specimens were prepared by

mechanical thinning to <150 μm, followed by precision ion polishing using a Gatan Precision Ion Polishing System (PIPS).

3. Results

3.1 Castability

The castability of the investigated alloys was evaluated in terms of fluidity and fading behaviour, which are critical parameters governing melt flow, mould filling and microstructural stability during casting. The combined assessment of these parameters provides insight into the processing characteristics of Sc-modified A356.2 alloys.

3.1.1 Fluidity Behaviour

The measured average fluidity lengths for all the alloys are presented in Figure 4. The results indicate a non-monotonic trend in fluidity with increasing Sc content. The baseline A356.2 alloy had a fluidity length of 50.66 ± 1.39 cm. With the addition of 0.2 wt.% Sc, a significant increase in fluidity was observed, reaching a maximum of 60.58 ± 4.28 cm, representing an increase of approximately 19.5%. The alloy with 0.4 wt.% Sc had a fluidity length of 54.34 ± 3.53 cm, which, whilst more than that of the baseline alloy, is lower than the alloy with 0.2 wt.% Sc. However, with a higher Sc content of 0.6 wt.%, the melt flow length decreased to 48.28 ± 3.97, which is lower than that of the baseline alloy.

Journal Pre-proof

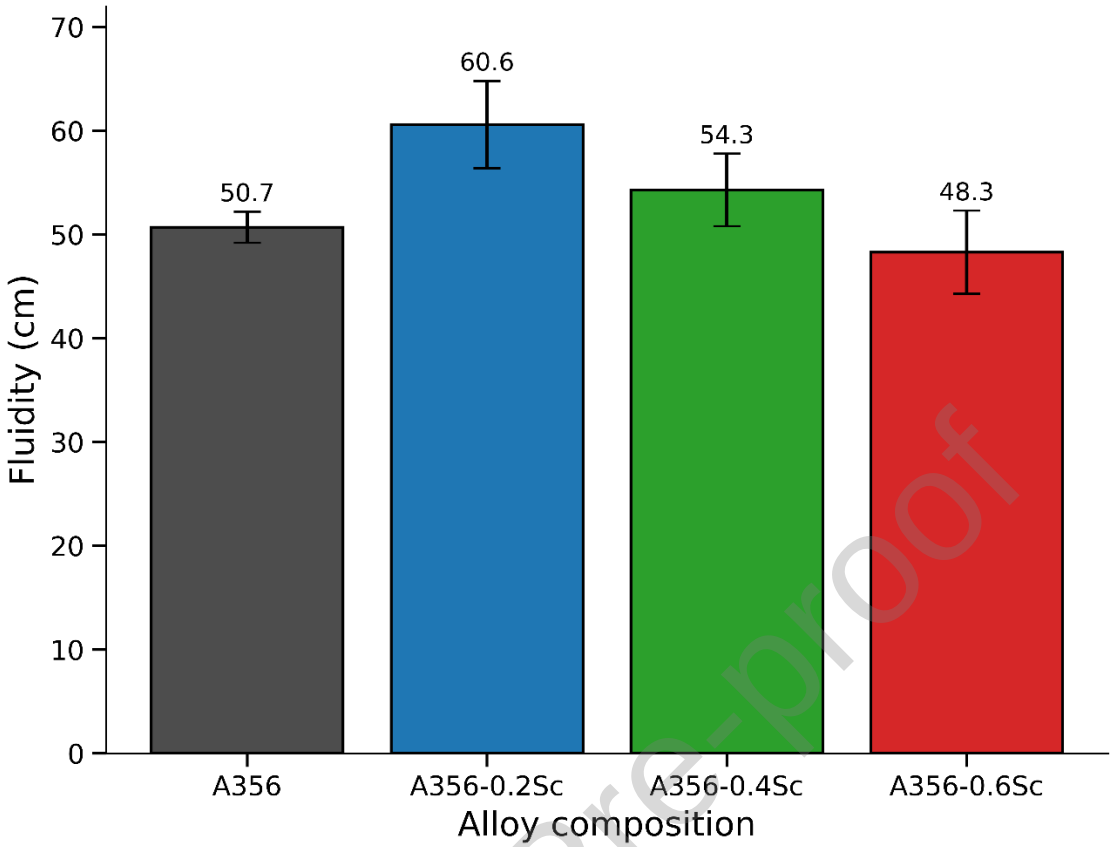


Figure 4 Variation of spiral fluidity length as a function of Sc content in A356.2 alloy. Error bars represent the standard deviation from seven measurements.

3.1.2 Fading Behaviour During Melt Holding

The effect of melt holding time on the grain size of the A356-0.4Sc is shown in Figure 5a, and the effect on mechanical properties is shown in Figure 5b. The complete anodised microstructure and the stress-strain curves for all tensile tests are provided in the Supplementary Material (Figure S1 and Figure S2). The results indicate that the Sc-modified alloy exhibits relatively stable grain-refinement behaviour during prolonged melt holding for up to 240 min. At the initial holding condition (0 min), the average grain size was measured as 345.25 ± 24 µm. A slight reduction in grain size was observed after 30 min of holding, reaching a minimum value of 320.47 ± 26 µm. With further increases in holding time, the grain size gradually increased to 330.73 ± 25 µm at 60 min and 340.53 ± 32 µm at 120 min. After prolonged holding of 180 and 240 min, the grain size moderately increased further to 360.55 ± 28 µm and 365.53 ± 29 µm, respectively. Despite the gradual increase over

Journal Pre-proof

extended holding times, the overall grain coarsening remained limited, indicating good resistance to fading during melt holding.

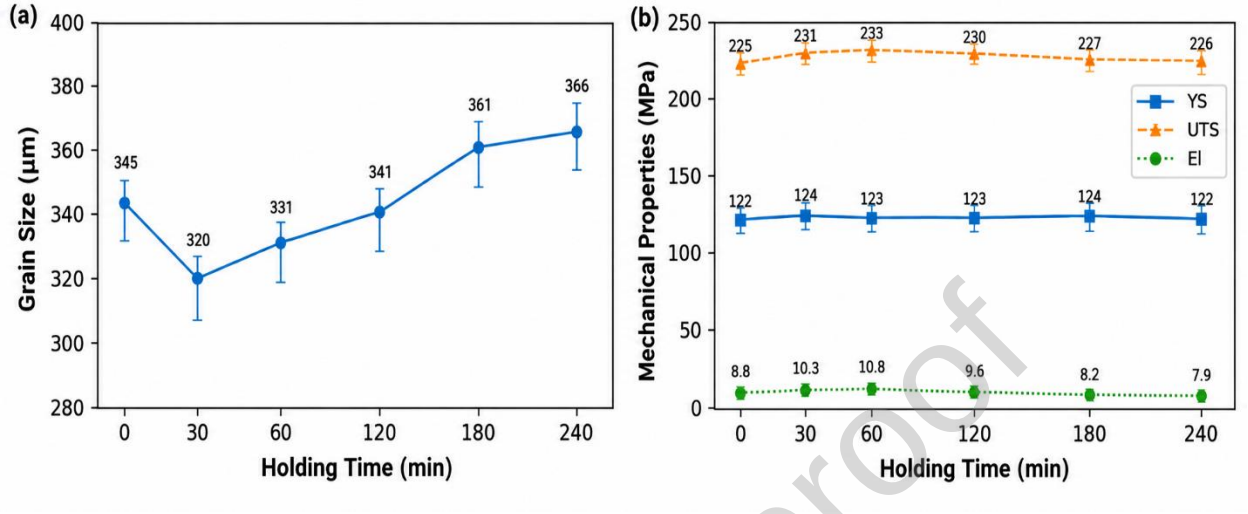


Figure 5 Effect of melt holding time on (a) grain size evolution and (b) mechanical properties (yield strength, ultimate tensile strength, and elongation) of A356-0.4Sc alloy.

The mechanical properties showed a trend consistent with the observed microstructural evolution. As can be seen from Table 2, the yield strength (YS) showed minimal variation, remaining within the range of 122-124 MPa for all holding times investigated. Similarly, the ultimate tensile strength (UTS) exhibited only minor fluctuations, increasing slightly from 225.28 MPa at 0 min to a maximum value of 232.89 MPa at 60 min, followed by a gradual decrease to 225.8 MPa after 240 min of holding. In contrast, elongation exhibited greater sensitivity to holding time. The elongation initially increased from 8.83% at 0 min to a maximum of 10.85% at 60 min, then gradually decreased to 7.92% after 240 min of holding. The density index (DI), used as an indicator of melt quality and hydrogen content, remains low throughout the holding period, with values of 0.2% at 0 and 30 min, increasing slightly to 0.4% at 60 min and 0.5% at 120-180 min, followed by a moderate increase to 1.4% at 240 min. The relatively low and nearly constant DI values up to 180 min suggest that melt quality remains largely stable during the initial holding period and therefore has a limited influence on the observed changes in mechanical properties. The actual tensile curves are provided in the Supplementary Materials.

Journal Pre-proof

Table 2 Evolution of grain size, DI, and mechanical properties with holding time

Time (min)	Grain Size (µm)	D.I.	YS [MPa]	UTS [MPa]	El (%)
0	345.25 ± 24	0.2	122.26	225.28	8.83
30	320.47 ± 26	0.2	124.25	230.8	10.29
60	330.73 ± 25	0.4	123.26	232.89	10.85
120	340.53 ± 32	0.5	122.99	230.3	9.57
180	360.55 ± 28	0.5	124.23	226.71	8.24
240	365.53 ± 29	1.4	122.5	225.8	7.92

3.2 Elevated Temperature Tensile Properties

The tensile properties of the A356-T6, A356-0.2Sc and A356-0.4Sc-T6 alloys at room temperature and 200 °C are presented in Figure 6 (Refer to Figure S3 in the supplementary material for the actual plot). The room-temperature tensile properties were obtained from the authors' previous study [4,5], while elevated-temperature tests of T6 treated alloys were conducted at 200 °C in the present study.

At room temperature, the A356-0.2Sc-T6 alloy exhibited the highest yield strength (YS) of 261.1 MPa and ultimate tensile strength (UTS) of 323.68 MPa, compared with 252.98 MPa and 305.96 MPa, respectively, for the baseline A356-T6 alloy. The elongation also increased from 6.23% for the baseline alloy to 9.47% with 0.2 wt.% Sc. In contrast, the A356-0.4Sc-T6 alloy showed a lower YS of 243.52 MPa than the baseline alloy, while its UTS remained higher at 319.45 MPa. Notably, the elongation increased further to 11.18%.

At 200 °C, both Sc-containing alloys retained higher tensile properties than the baseline alloy. The YS increased from 181.68 MPa for A356-T6 to 195.89 MPa for A356-0.2Sc-T6 and 185.76 MPa for A356-0.4Sc-T6. Similarly, the UTS increased from 212.81 MPa for the baseline alloy to 218.62 MPa and 215.08 MPa for the 0.2 and 0.4 wt.% Sc alloys, respectively. The improvement in ductility was more pronounced, with elongation increasing from 12.21% for the baseline alloy to 15.98% for A356-0.2Sc-T6 and 17.88% for A356-0.4Sc-T6. Thus, at 200 °C, the 0.2 wt.% Sc alloy provided the highest strength, whereas the 0.4 wt.% Sc alloy provided the highest elongation.

Journal Pre-proof

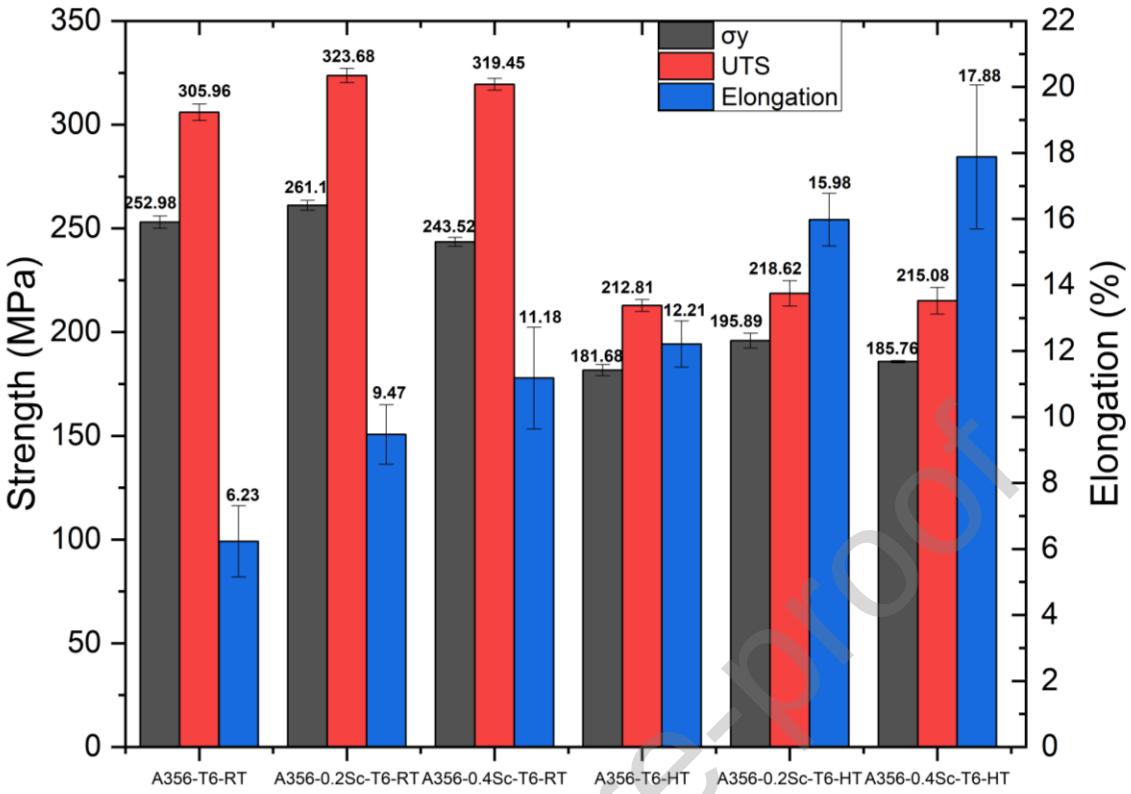


Figure 6 Room temperature and elevated temperature tensile properties of A356, A356-0.2Sc and A356-0.4Sc alloys tested at 200 °C, showing yield strength (YS), ultimate tensile strength (UTS), and elongation (El) with corresponding error bars.

3.3 Fatigue Performance

The high cycle fatigue (HCF) behaviour of the A356-T6 and A356-0.2Sc-T6 alloys was evaluated under stress-controlled conditions, and the results are presented in the form of S-N curves as shown in Figure 7. The applied stress amplitudes were selected based on the yield strength of the baseline A356.2 alloy in the T6 condition. The yield strength of A356-T6 was 252.98 MPa, as shown in Figure 6. The stress amplitudes were chosen in the range of 30% to 70% of this value (75.6-176.4 MPa), enabling a systematic evaluation of fatigue behaviour from low to high stress ranges.

At the lowest applied stress amplitude of 75.6 MPa (30% of YS), neither alloy failed after 10^7 cycles, and these specimens were therefore classified as run-outs. This indicates that the applied stress lies below the fatigue endurance limit under the present testing conditions. With increasing stress amplitude, a progressive reduction in fatigue life was observed for

both alloys. For the A356-T6 alloy, the fatigue life increased from approximately 1.08×10^5 cycles at a stress amplitude of 176.4 MPa to 2.46×10^6 cycles at 88.2 MPa. The A356-0.2Sc-T6 alloy had fatigue lives ranging from approximately 1.02×10^5 cycles at 176.4 MPa to 4.83×10^6 cycles at 88.2 MPa.

Overall, the Sc-containing alloy exhibited higher fatigue lives at several of the investigated stress amplitudes, although noticeable scatter was observed and the fatigue response was not consistently improved at all stress levels. For example, at a stress amplitude of 151.2 MPa, the baseline alloy exhibited a fatigue life of approximately 2.19×10^5 cycles, whereas the Sc-containing alloy failed at approximately 1.05×10^5 cycles.

The relationship between stress amplitude and fatigue life was further analysed using Basquin's equation [11] :

$$\sigma_a = \sigma_f'(2N_f)^b \qquad (1)$$

where σ_a is the applied stress amplitude, σ'_f is the fatigue strength coefficient, $2N_f$ represents the number of stress reversals to failure and b is the fatigue strength exponent.

The fitted Basquin equations obtained for the studied alloys are given as:

$$\sigma_a = 2763.7(2N_f)^{-0.229} \qquad (2)$$

for the A356-T6 alloy, and

$$\sigma_a = 1292.6(2N_f)^{-0.168} \qquad (3)$$

for the A356-0.2Sc-T6 alloy.

The corresponding coefficient of determination (R^2) values were 0.905 and 0.873 for the A356-T6 and A356-0.2Sc-T6 alloys, respectively, indicating good agreement between the experimental data and the fitted Basquin relationships.

Journal Pre-proof

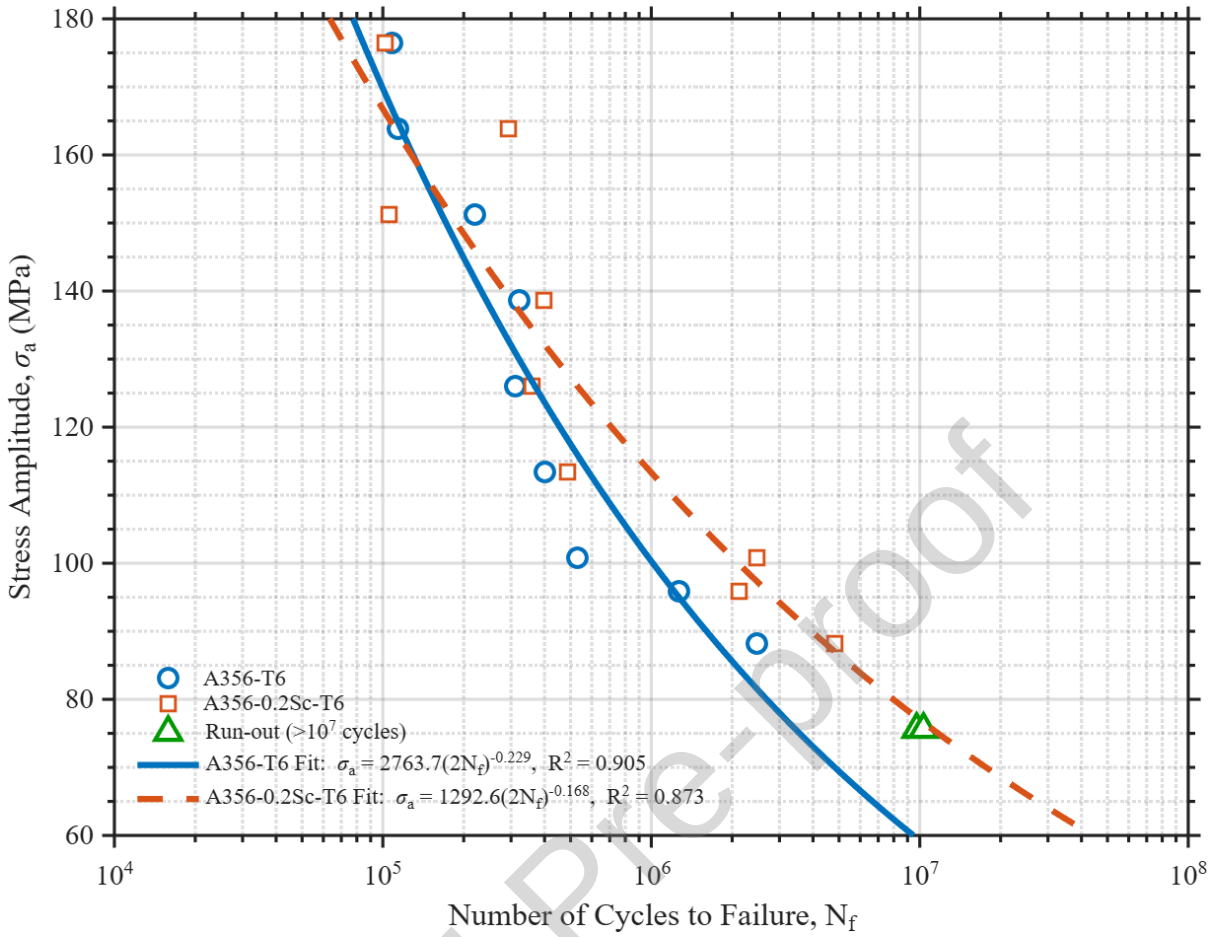


Figure 7 S-N curves of the A356-T6 and A356-0.2Sc-T6 alloys under axial fatigue loading conditions. Blue and orange lines represent Basquin fitting relationships, while triangular markers indicate runout conditions at 10^7cycles at a stress amplitude of 75.6 MPa for both alloys.

Fractography analysis of the fatigue-tested specimens was carried out to identify crack initiation, crack propagation and final overload fracture regions. The SEM fractography images of the fatigue-tested A356-T6 and A356-0.2Sc-T6 alloys at stress amplitudes corresponding to 40% and 70% of the yield strength are presented in Figure 8 and Figure 9 respectively. Fatigue cracks were predominantly initiated at or near the specimen surface, from where they propagated progressively across the cross-section before final failure occurred.

Journal Pre-proof

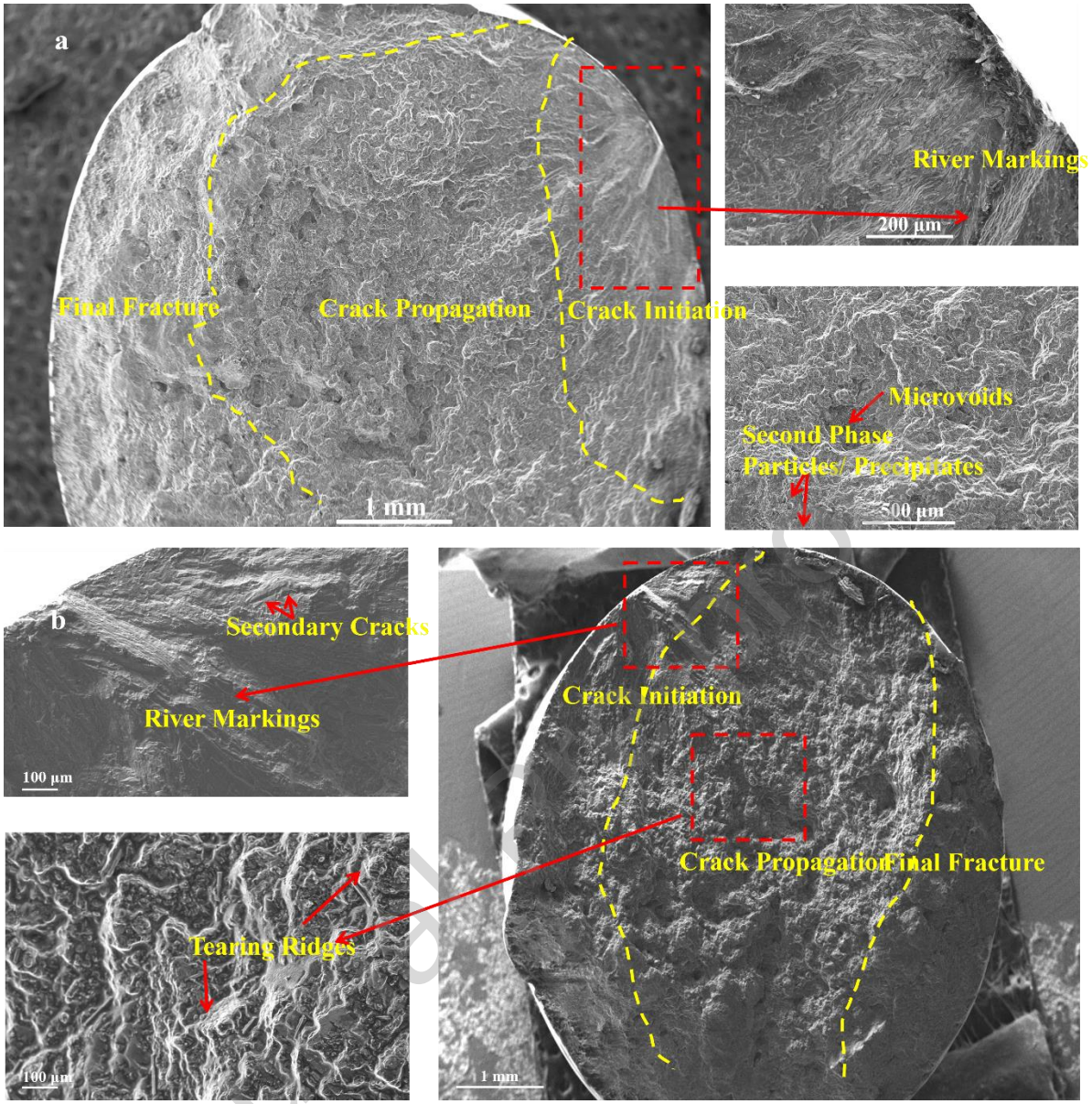


Figure 8 SEM micrographs showing the fatigue fracture surface subjected to the stress amplitude of 40% of the YS of the baseline alloy for: a) A356; and b) A356-0.2Sc alloys.

For the A356-T6 alloy tested at a stress amplitude equivalent to 40% YS, a distinct crack initiation site was identified at the specimen edge, followed by a broad fatigue crack propagation region characterised by fatigue crack growth markings. Several particle-associated features, which could be secondary phases or precipitates, were observed within the propagation zone. The final overload fracture region exhibited a comparatively rough morphology, indicating rapid fracture after extensive crack propagation. Under the same loading conditions, the A356-0.2Sc-T6 alloy exhibited a similar fracture sequence; however, the propagation region featured more pronounced tearing ridges and localised secondary cracks. Fatigue crack growth markings extended over a substantial portion of the fracture

surface before transitioning into the final overload region.

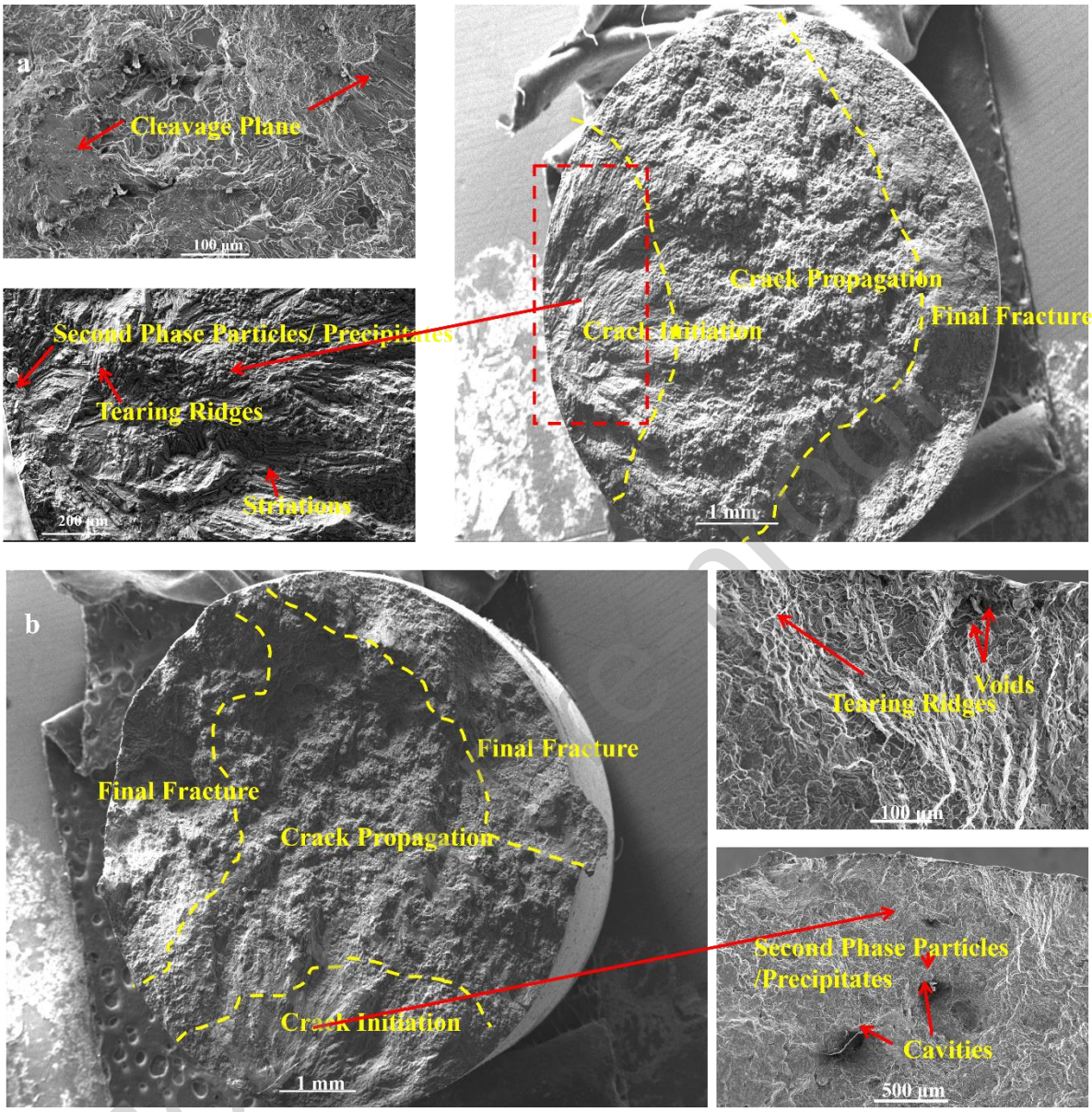


Figure 9 SEM micrographs showing the fatigue fracture surface subjected to the stress amplitude of 70% of the YS of the baseline alloy for: a) A356; and b) A356-0.2Sc alloys.

At a 70% YS stress amplitude value, the fracture surface of the A356-T6 alloy exhibited a clearly defined crack initiation region followed by crack propagation through the central portion of the fracture surface. Numerous cavities and void-like defects were observed within both the initiation and propagation regions, together with particle-associated features distributed along the crack path. Higher-magnification observations revealed pronounced tearing ridges and additional void-like features. Notably, two distinct final overload fracture regions were observed on opposite sides of the fracture surface, separated by the central

fatigue crack propagation zone. In contrast, the A356-0.2Sc-T6 alloy tested at 70% YS exhibited a well-defined crack initiation site followed by a broad fatigue crack propagation region and a final overload fracture zone. Fatigue crack growth markings, tearing ridges, secondary phases/precipitates associated features, and isolated cleavage-like facets were observed within the propagation region, while the final overload region exhibited a rough fracture morphology characteristic of rapid final failure.

To compare the influence of Sc addition on casting-related defects under non-degassed conditions, quantitative image analysis was performed on the A356 and A356-0.2Sc alloys. The corresponding optical micrographs are shown in Figure 10. The same metallographic imaging and image-analysis procedure was applied to both alloys. The samples examined were deliberately cast without degassing to investigate the effect of Sc addition on casting-related defects under non-degassed conditions. This approach was adopted to minimise the additional variability associated with differences in melt quality between separate melting and casting trials, particularly because achieving comparable density index (DI) values across different melts can be challenging. Accordingly, Figure 10 compares the relative defect populations of the two alloys under non-degassed conditions and is not intended to assess degassing efficiency. These samples were used exclusively for defect analysis and were not used for the fatigue tests reported in this study. Therefore, the defect populations shown in Figure 10 should not be interpreted as directly representing the defects responsible for the fatigue behaviour discussed in Figure 7.

Journal Pre-proof

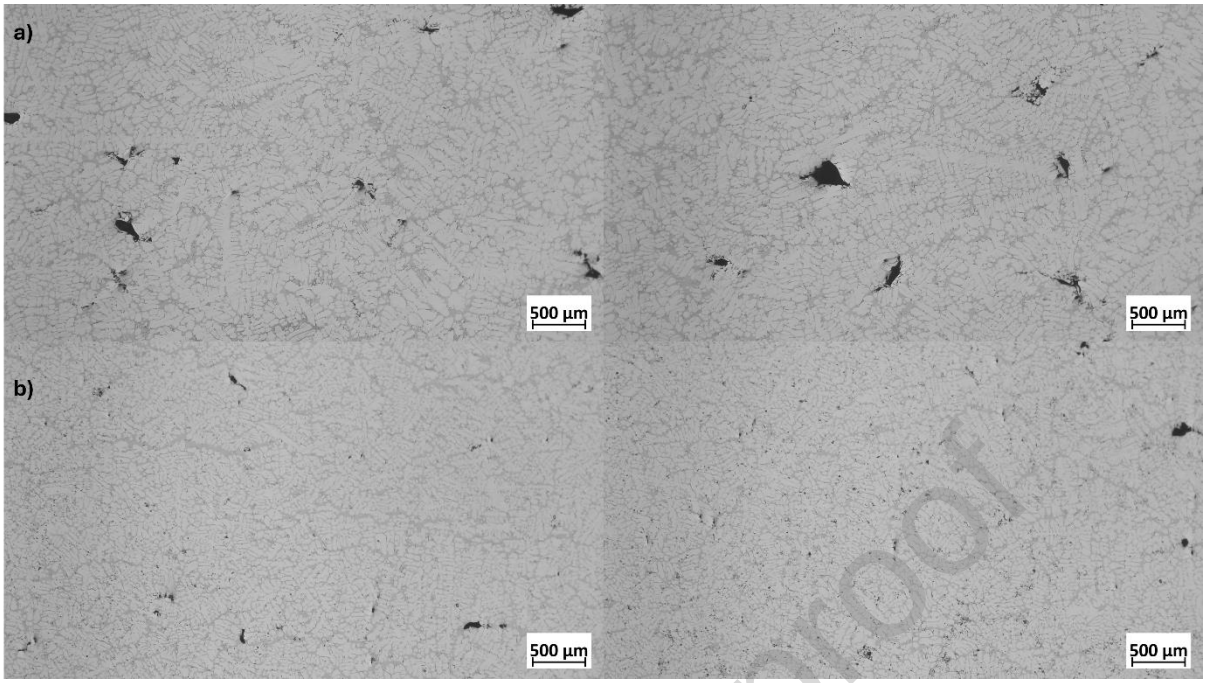


Figure 10 Optical micrographs showing casting-related porosities in (a) A356 and (b) A356-0.2Sc alloys. The images were analysed using ImageJ to quantify the area fraction and characteristic size of the detected defects.

The quantitative results obtained from the ImageJ analysis are summarised in Table 3. The A356 alloy exhibited a higher measured area fraction of porosities than the A356-0.2Sc alloy, with values of 0.51 ± 0.09% and 0.35 ± 0.03%, respectively. The mean Feret diameter of the detected features decreased from 113.90 ± 21.77µm for A356 to 101.37 ± 25.83 µm for A356-0.2Sc. The maximum Feret diameter also decreased from 286.43 µm for A356 to 202.72 µm for A356-0.2Sc. Thus, the addition of 0.2 wt.% Sc was associated with a lower measured area fraction and smaller characteristic size of the detected casting-related porosities.

Table 3 Quantitative analysis of porosity defects in the investigated A356-based alloys.

Alloy	Area Fraction (%)	Mean Feret Diameter (µm)	Maximum Feret diameter (µm)
A356	0.51 ± 0.09	113.90 ± 21.77	286.43
A356-0.2Sc	0.35± 0.03	101.37 ± 25.83	202.72

Journal Pre-proof

4. Discussion

4.1 Effect of Sc Addition on Solidification Behaviour, Fluidity and Grain Refinement

The fluidity results as shown in Figure 4 demonstrated that the addition of Sc up to 0.2 wt.% resulted in a 19.5% increment in the fluidity compared to the baseline alloy. Further increasing the Sc content to 0.4 wt.% reduced fluidity compared to 0.2 wt.% Sc alloy. However, the fluidity remained approximately 7.1% higher than that of the baseline alloy. In contrast, the alloy containing 0.6 wt.% Sc exhibited the lowest fluidity, approximately 4.7% lower than the baseline alloy. These results indicate that the addition of Sc significantly influences the fluidity of the A356 alloy, with the highest fluidity at 0.2 wt.% Sc.

In general, fluidity is controlled by a combination of multiple factors, which can be divided into two categories: (i) metallurgical factors such as the alloy composition, latent heat, surface tension, viscosity and solidification kinetics including grain refinement, eutectic modification and formation of intermetallic phases; and (ii) casting variables such as cooling rate, degree of superheat, mould material and coating, casting temperature and casting defects [12].

In the context of the current study, the influence of Sc additions on solidification behaviour and microstructure are considered influencing factor on the fluidity of the A356.2 alloy, as all other parameters were held constant across all alloys studied. In particular, grain refinement is one of the major factors influencing an alloy's fluidity. However, in this regard, there are some inconsistencies in studies into the relationship between grain refinement on fluidity, with some studies showing a positive effect, whereas others show no or a negative impact of grain refinement on the fluidity. For instance, Mollard et al. [13] observed a decrease in fluidity with the addition of 0.15% Ti to the Al-4.5Cu alloy, whilst Tiryakioglu et al. [14] found no effect of grain refinement due to 0.04 wt.% Ti addition on the fluidity of A356 alloy. In contrast, Dahle et al. [15] observed that in A356 alloy with Al-5Ti-B grain refiner, with less than 0.12 wt.% Ti, the fluidity decreased, whereas it increased with more than 0.12 wt.% Ti. These findings indicate that the amount and type of grain refiner also contribute significantly to an alloy's fluidity, along with the alloy composition. Contrarily, Kwon et al. [16] found that with 0.03 wt.% Ti addition through Al-5Ti-B grain refiner in A356 alloy, the fluidity was improved. Similarly, Lang et al. found a considerable improvement in fluidity by adding 0.04 to 0.07 wt.% B to Al-Si alloys.

Journal Pre-proof

As can be seen from Figure 11, the grain size reduces considerably with Sc addition from 540 μm in the baseline A356.2 alloy to 338 μm in the 0.2Sc alloy, 260 μm in the 0.4Sc alloy and 413 μm in the 0.6Sc alloy. The secondary dendrite arm spacing (SDAS) was also reduced from 24.10 ± 3.05 μm in the baseline alloy to 22.55 ± 2.24 μm for 0.2 wt.% Sc, 19.73 ± 1.94 for 0.4 wt.% Sc and 22.45 ± 1.82 for 0.6 wt.% Sc. The addition of Sc resulted in a larger number of fine equiaxed grains and suppressed growth of coarse dendrites. In particular, the alloy with 0.2 wt.% and 0.4 wt.% Sc resulted in the finest grain size and SDAS, thereby improving fluidity compared to the baseline alloy. The relationship between grain refinement and fluidity is generally explained in terms of the dendrite coherency point. The dendrite coherency point is a point during solidification, where individual dendrites first impinge upon the neighbouring dendrites, forming a network [17]. In non-refined alloys, large, elongated dendrites form and interlock early in the solidification process, creating a rigid network that blocks the flow of remaining liquid. Grain refinement postpones dendrite coherency and this delayed dendrite interlocking allows the liquid metal to flow over longer distances before solidification arrest occurs [18]. Consequently, factors that delay dendrite coherency generally improve fluidity, whereas factors that accelerate solid network formation reduce the filling capability of the melt. Similar improvements in fluidity associated with the increase in the temperature interval of coherency and coherency time and delay in dendrite coherency due to Al-5Ti-B grain refiner have been reported by Malekan et al. [19].Yang eta al. [20] also observed the same by adding Si and Ni in Al-Ni-Si alloys.

Another important factor influencing the fluidity of Al-Si hypoeutectic alloys is the modification of plate-like coarse silicon particles to fibrous particles. There are multiple aspects to Si modification that impact fluidity. Firstly, fluidity is usually determined by changes during the initial stages of solidification; hence, the effect of eutectic modifiers is expected to have less impact on fluidity [12,21]. Secondly, experimental investigations have shown that, with the addition of these modifying agents, the eutectic temperature decreases and the undercooling of eutectic Si increases [5,22], suggesting that the melt has a longer flow time during solidification, thereby improving fluidity. As discussed above fluidity is also impacted by the growth, convergence and interlock of secondary dendrites during solidification. In addition, the modification of eutectic Si alters its morphology and increases the number of dendrite junctions, thereby influencing the fluidity [21,22]. Some studies found that the addition of Na and Sr, individually and together, and with Ti, reduced the fluidity of the alloy [23–25]. On the other hand, some studies show the positive effect of eutectic Si

modification by Sr modification [26,27]. As reported previously, Sc addition modifies the morphology of eutectic Si [4,5] and could therefore help improve the fluidity of A356 alloy.

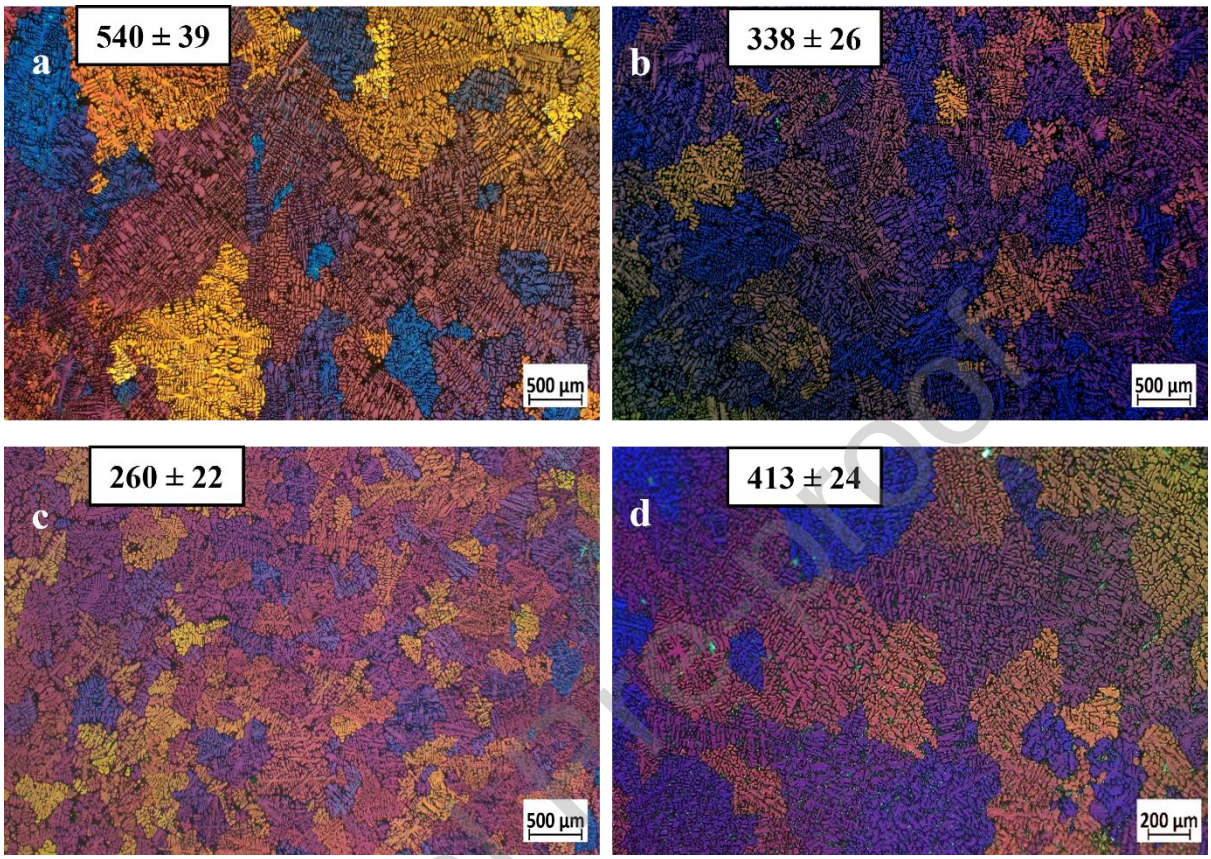


Figure 11 Optical Micrographs showing the variation of grain size in (a) A356.2; (b) A356-0.2Sc; (c) A356-0.4Sc; and (d) A356-0.6Sc alloys in as cast conditions under polarised light with anodised surface

Several other secondary factors may improve the fluidity of Sc-modified alloys. For example, the modification of the morphology of β-Al5FeSi from needle-like to a more nodular form could impact fluidity. As reported by Taghaddos et al. [28], the Mn-modified melts exhibited greater fluidity than the unmodified ones. Sc addition is also known to modify the Fe intermetallic [29–31] and thereby improving the melt's fluidity to some extent. Figure 18 also shows the modification in the morphologies of these intermetallics. These large and coarse intermetallic particles restrict interdendritic connections during feeding.

The present results suggest that 0.2 wt.% Sc provides sufficient grain refinement to delay dendrite coherency without significantly increasing the volume fraction of $AlSc_2Si_2$ intermetallics present in the flowing melt. However, further increases in Sc content did not produce additional improvements in fluidity despite continued grain refinement. The A356-

0.4Sc alloy exhibited the finest grain structure among all investigated compositions, yet its fluidity remained lower than that of the A356-0.2Sc alloy. This behaviour indicates that secondary effects associated with Sc addition become increasingly important at higher concentrations.

Thermodynamic calculations provide useful insight into the possible origin of these effects. The equilibrium phase fraction calculations shown in Figure 12 predict the formation of $AlSc_2Si_2$ in all Sc-containing alloys, with the predicted fraction increasing progressively with Sc content, from approximately 0.3% in A356-0.2Sc to 0.6% and 0.94% in A356-0.4Sc and A356-0.6Sc, respectively. An increasing volume fraction of Sc-containing intermetallic phases may increase the effective solid fraction within the mushy zone and consequently increase the resistance to liquid flow [28]. However, because these calculations represent equilibrium conditions, the predicted phase fractions should not be interpreted as the actual phase fractions present during the transient spiral-filling process. Rather, they provide an indication of the thermodynamic tendency for increased Sc-containing phase formation with increasing Sc content.

Journal Pre-proof

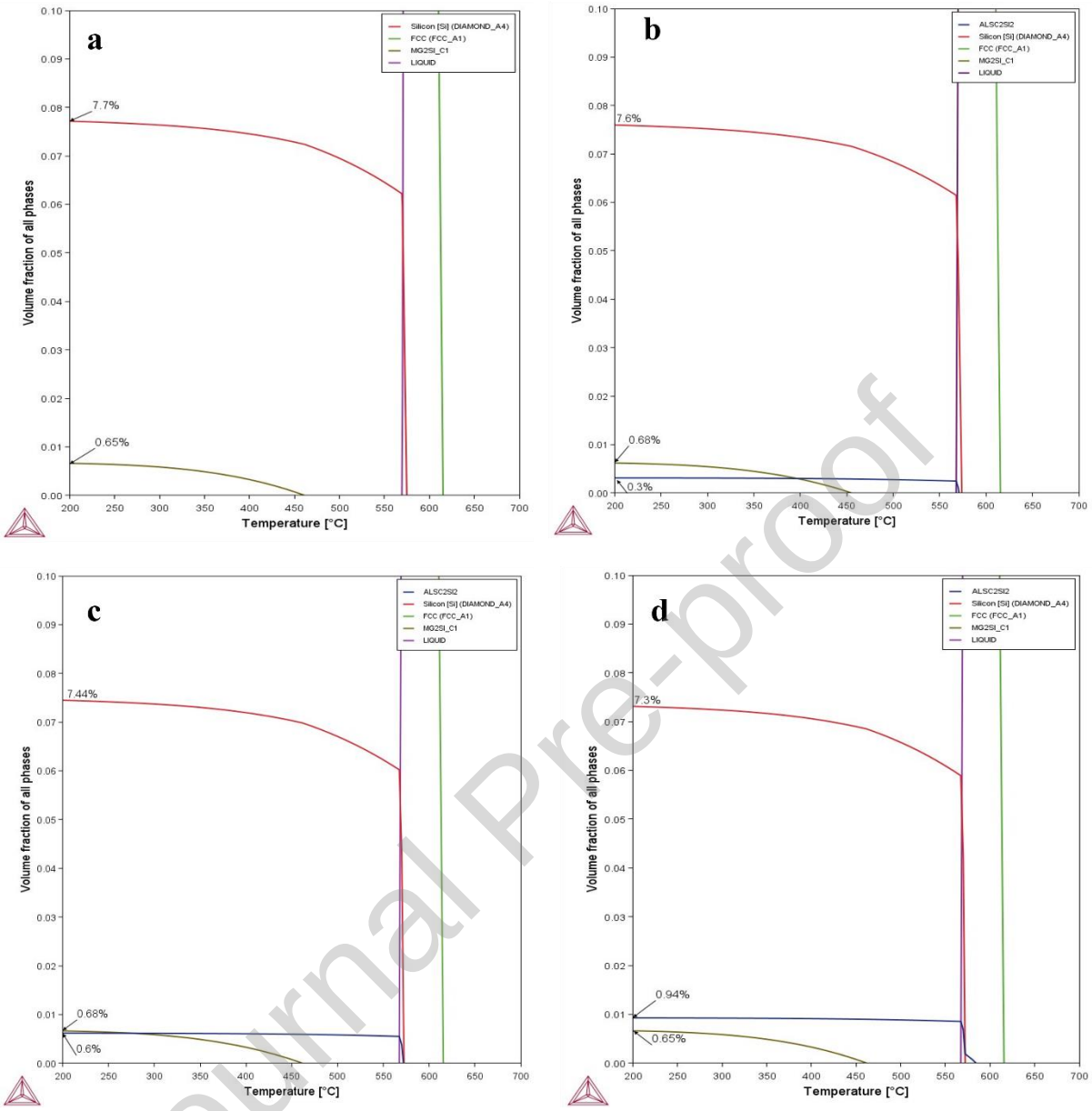


Figure 12 Equilibrium volume fraction calculations for the solidification of: (a) A356; (b) A356-0.2Sc; (c) A356-0.4Sc; and (d) A356-0.6Sc alloys. The calculated equilibrium fraction of $AlSc_2Si_2$ intermetallic increases with increasing Sc content.

Consequently, the beneficial effect of grain refinement may be increasingly counteracted by the greater population of Sc-containing intermetallic phases at higher Sc contents. This provides a possible explanation for why the A356-0.6Sc alloy exhibited the lowest fluidity despite possessing a finer grain structure than the baseline alloy and why the A356-0.4Sc alloy had lower fluidity than the A356-0.2Sc alloy. The SEM micrographs in Figure 13 show

Journal Pre-proof

the presence of relatively coarse intermetallics in the higher-Sc alloy, providing complementary microstructural evidence for this interpretation.

In the previous study, it was shown that beyond 0.54 wt.% Sc, primary $AlSc_2Si_2$ intermetallic starts to form along with α-Al, which are moderately coarse in nature [5] and can be observed in Figure 13c. At this Sc level, the increased amount of Sc-containing intermetallics, together with the predicted changes in the solidification interval, may promote earlier development of a semi-solid network, thereby restricting melt flow and reducing the achievable filling length. Similar behaviour has been reported in A356-Ce alloys [32], where grain refinement and eutectic modification improve the fluidity of the alloy up to 0.5 wt.% Ce and beyond this, the fluidity is dramatically reduced due to the formation of Al-20Si-10Mg-3Fe-Ce and Al-17Ce-12Ti-2Si intermetallic phases.

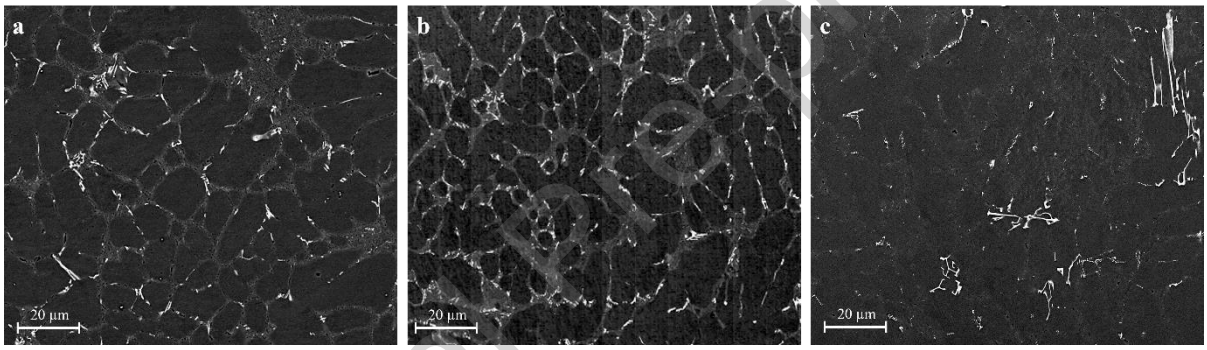


Figure 13 SEM micrographs showing the intermetallics in: (a) A356; (b) A356-0.2Sc; and (c) A356-0.6Sc alloys. The coarser primary intermetallics are responsible for the decrease in fluidity of the alloy with 0.6 wt.% Sc.

Similar improvements in fluidity at low Sc additions have been reported in the literature. According to Puparattanapong et al.[33] and Prukkanon et al. [34] variation in fluidity lengths were observed relative to Sc content: A356-0.2Sc > A356-0.4Sc > A356. Similarly, Mao et al. [35], also suggested that A357-0.2Sc alloy had improved fluidity relative to the baseline A357 and A357-Sc-Zr alloy. However, none of these papers comprehensively addressed the balance between beneficial grain refinement, Si modification and detrimental intermetallic formation.

Overall, the results indicate that the fluidity response varies non-monotonically with increasing Sc content. The improved fluidity at 0.2 wt.% Sc is associated with the beneficial

effects of grain refinement and eutectic modification, whereas further Sc addition does not provide additional improvement. The reduced fluidity at higher Sc contents may be related to the increasing formation of Sc-containing intermetallic phases and changes in the solidification behaviour. It should be noted, however, that the measured Si, Mg and Ti contents also vary slightly with Sc content (Table 1), and these compositional variations may contribute slightly to the observed differences in solidification and fluidity. Therefore, the present results demonstrate a composition-dependent response associated with increasing Sc content, but the individual contribution of Sc cannot be completely isolated from the minor variations in the other alloying elements. Furthermore, the CALPHAD results provide equilibrium thermodynamic guidance rather than a direct description of the transient, non-equilibrium phase evolution during spiral filling.

4.2 Fading resistance and its impact on microstructure-property evolution in A356-0.4Sc alloy

Grain refinement is widely used in Al-Si casting alloys to improve casting quality and mechanical properties by promoting a fine equiaxed grain structure. Commercial grain refiners such as Al-Ti-B and Al-Ti-C have been used extensively for this purpose. However, one of the primary limitations of these grain refiners in Al-Si casting alloys is the gradual loss of grain-refining efficiency during prolonged melt holding, commonly referred to as grain-refiner fading. This phenomenon has been extensively reported and is generally attributed to the settling and agglomeration of TiB_2 particles [36], together with the well-known Si-poisoning effect, in which dissolved Si reacts with Ti, reducing the availability of active Ti solute required to maintain the nucleation potency of TiB_2 particles [37,38]. As a result, prolonged holding typically leads to progressive grain coarsening and deterioration of mechanical properties.

To overcome these limitations, several alternative grain refinement systems have recently been proposed. Silva Jr. et al. [39] demonstrated that Al-Nb-B master alloys exhibit significantly improved resistance to fading till 60 minutes due to the NbB2 particles remaining stable in the Al-Si melt and hence not being susceptible to the severe Si-poisoning mechanism characteristic of Ti-based grain refiners. Similarly, Zhou et al. [40] reported that Al-V-B master alloys retained effective grain refinement for up to 240 min of melt holding through the formation of thermally stable V-containing compounds, while Ran et al. [41]

showed that Al-Ti-V-B master alloys exhibit enhanced refinement stability with a minimal increase in grain size till 70 minutes, owing to the evolution of stable (Ti, V)-containing nucleating phases. These studies indicate that improving the thermodynamic stability of heterogeneous nucleation particles is an effective strategy for mitigating grain refiner fading. However, these studies primarily focused on the evolution of grain size during melt holding, while the correlation between grain refinement stability and the retention of mechanical properties was not systematically investigated. Hence, the long-term effectiveness of these grain refiners in maintaining both microstructural refinement and mechanical performance remains to be fully established.

In the present study, the Sc-modified A356 alloy maintained relatively stable grain size during prolonged melt holding under the experimental conditions. As shown in Figure 5a, the average grain size decreased slightly from 345.25 ± 24 μm under the initial condition (just after degassing) to 320.24 ± 27 μm after 30 min of holding, suggesting that the grain-refining effect became fully established during the early stages of melt holding. Thereafter, the grain size increased only gradually with increasing holding time, reaching 340.53 ± 32 μm after 120 min and 365.43 ± 29 μm after 240 min. Despite the extended holding period, the overall increase in grain size between 30 and 240 min was only approximately 14%, and between 0 and 240 min was approximately 6%, indicating that the grain-refining efficiency was largely retained even after four hours of melt holding. Furthermore, the overlapping error bars indicate that the observed grain coarsening was relatively modest. For comparison, the grain-size evolution reported for conventional Al-Ti-B [9,36], Al-Ti-C [42] and Al-Sr-B [43,44] grain refiners has been extracted and replotted in Figure 14. The literature data provide useful qualitative context for the present fading behaviour; however, the reported results were obtained using different alloy compositions, grain-refiner additions, holding temperatures, holding times and cooling conditions. Therefore, the data in Figure 13 should not be interpreted as a strict quantitative comparison of fading resistance between different grain-refining systems. Within these limitations, the present Sc-modified A356 alloy shows

Journal Pre-proof

relatively limited grain coarsening over the investigated 240 min holding period.

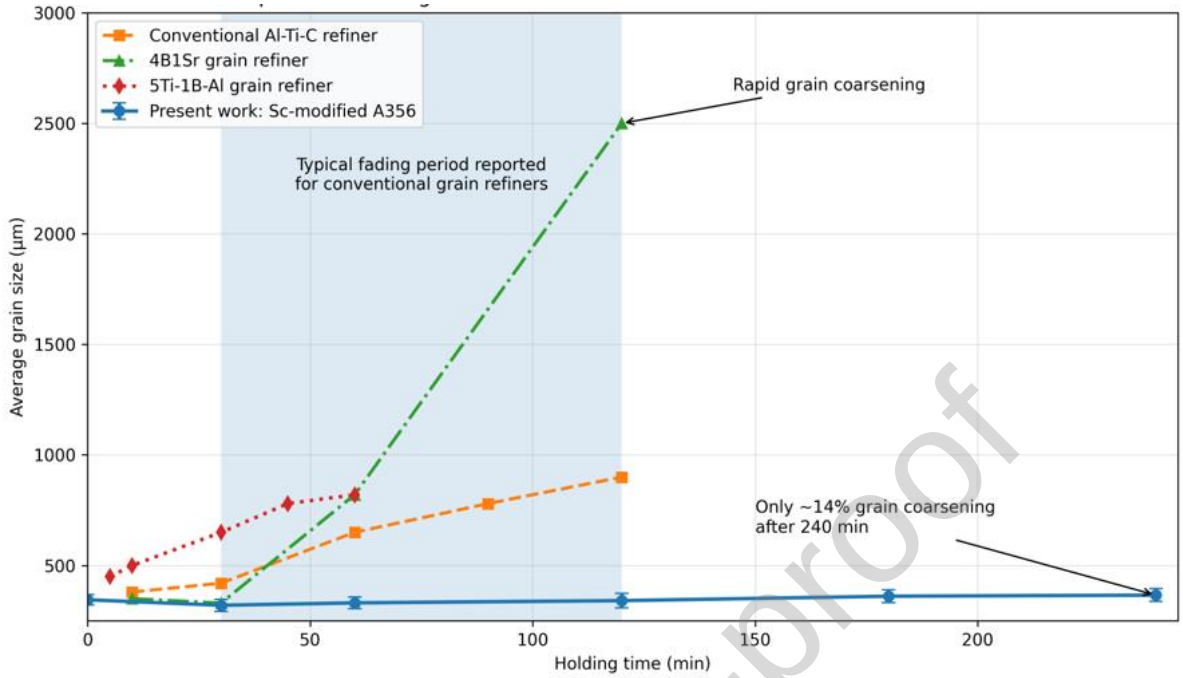


Figure 14 Qualitative comparison of grain-size evolution during melt holding for the present Sc-modified A356 alloy and selected literature data for conventional grain-refining systems. Literature data for Al-Ti-B, Al-Ti-C and Al-Sr-B grain refiners were extracted from Refs. [9,36,42–44].

The relatively small change in grain size was reflected in the tensile properties of the alloy. As shown in Figure 5b, the yield strength remained essentially unchanged across the various holding periods, fluctuating only between 122.26 and 124.25 MPa, while the ultimate tensile strength varied within a narrow range of 225.28-232.89 MPa. These minor variations fall within the normal scatter expected for cast aluminium alloys and indicate that prolonged melt holding did not significantly degrade the alloy's strength. In contrast, elongation gradually decreased from 10.32% at 30 min to 7.92% after 240 min of holding. This reduction in ductility coincided with a gradual increase in the D.I. from 0.2 to 1.1, indicating a slight deterioration in melt quality during prolonged holding. The D.I. is widely used as an indicator of the melt's susceptibility to gas porosity, with increasing D.I. values generally reflecting higher hydrogen content and/or a greater tendency for pore formation. Although the melt was protected using an argon atmosphere, prolonged holding can still result in limited hydrogen absorption and minor oxide entrainment during melt handling, leading to a gradual increase in D.I. These defects have a greater influence on ductility than on strength because they act as

preferential sites for void nucleation and crack initiation during plastic deformation [45]. Consequently, while the yield strength and ultimate tensile strength remained essentially unaffected, the slight increase in D.I. provides a reasonable explanation for the gradual reduction in elongation observed after extended melt holding.

The relatively stable grain size observed during prolonged melt holding may be associated, at least in part, to the formation of stable Sc-containing heterogeneous nucleation particles during solidification that retain their effectiveness during prolonged melt holding. Previous studies have shown that, in Al-7Si-based cast alloys, $(Al, Si)_3(Ti, Sc)$ phase is formed during solidification instead of the conventional Al_3Sc phase [5,46,47]. This phase is considered a derivative of the $L1_2$ - Al_3Sc structure through the substitution of Si and Ti atoms and has been identified as an effective heterogeneous nucleation substrate for primary α-Al [5]. Recent work by Lian et al. [46] further showed that the formation of $(Al, Si)_3(Ti, Sc)$ fundamentally modifies the grain refinement mechanism in Al-Si alloys by suppressing the conventional Si-poisoning effect associated with Al-Ti grain refiners. Instead of allowing Ti to participate in detrimental Ti-Si reactions, Sc promotes the formation of stable Sc-Ti-containing particles that retain high heterogeneous nucleation potency during solidification. Similarly, Mao et al. [47] reported that these Sc-containing particles remain effective heterogeneous nucleation sites over a wide range of cooling conditions, thereby mitigating the Si-poisoning effect that typically limits the performance of conventional Al-Ti-B grain refiners. In the authors' previous study [5], TEM analysis confirmed the presence of the $(Al, Si)_3(Ti, Sc)$ phase in the as-cast condition. Combined with the limited grain coarsening observed after 240 min of melt holding in the present study, these findings suggest that the formation of stable $(Al, Si)_3(Ti, Sc)$ particles may contribute to maintaining heterogeneous nucleation efficiency during prolonged melt holding, potentially mitigating the Si-poisoning effects associated with conventional Al-Ti-based grain refiners.

More importantly, the present observations are consistent with the underlying mechanism proposed for several recently developed grain refiners, which are more resistant to fading. For example, Nb-B refiners maintain their grain-refining efficiency through the formation of stable Al_3Nb/NbB_2 nucleation particles that have slower dissolution kinetics and are immune to the conventional Si-poisoning mechanism associated with Al-Ti-B refiners [39]. Similarly,

V-containing grain refiners derive their superior fading resistance from the formation of stable (Ti,V)Al_3 and (Ti,V)B_2 or VB_2 particles, which retain high nucleation potency and effectively suppress the degradation of refinement efficiency during prolonged melt holding [40,41]. Although the chemistry of the present Sc-modified alloy differs from that of these master alloys, the underlying mechanism appears to be similar. Unlike Nb- and V-based grain refiners, where the gradual loss of refinement efficiency after approximately 60-70 min has been attributed primarily to particle sedimentation and agglomeration [39,41], the present Sc-modified alloy exhibited only a modest increase in grain size after 240 min of melt holding. Although particle sedimentation or agglomeration was not directly investigated in the present work, the retained grain refinement suggests that these mechanisms, if present, had only a limited influence on the effectiveness of the Sc-containing nucleation particles under the present processing conditions. To the best of the authors' knowledge, there are very few studies evaluating the fading behaviour of Sc-containing grain refiners in Al-Si casting alloys. Pramod et al. [48] reported no significant fading effect in Sc-containing A356 alloys for 120 minutes. However, their assessment was based primarily on optical micrographs, without presenting images of anodised grain structure or quantitative grain-size measurements to directly evaluate the evolution of the primary α-Al grain structure, or a systematic evaluation of mechanical properties. In contrast, the present study provides a more comprehensive assessment by correlating grain size, tensile properties, and holding time. From an industrial perspective, this behaviour is particularly advantageous because casting operations frequently involve prolonged melt holding during production.

4.3 Elevated-Temperature Tensile Behaviour and Strength Retention Mechanisms

The tensile behaviour of the T6-treated alloys as shown in Figure 6 shows that at ambient temperature, A356-0.2Sc exhibited the highest strength, with YS and UTS of 261.10 and 323.68 MPa, respectively, compared with 252.98 and 305.96 MPa for the baseline A356 alloy. Increasing the Sc content to 0.4 wt.% did not provide a further improvement in ambient-temperature strength. Instead, the YS decreased to 243.52 MPa, below that of the baseline A356 alloy, although the UTS remained comparatively high at 319.45 MPa.

At elevated temperature of 200 °C, the baseline A356 alloy exhibited YS and UTS values of 181.68 and 212.81 MPa, respectively, whereas A356-0.2Sc retained the highest YS and UTS of 195.89 and 218.62 MPa. A356-0.4Sc exhibited intermediate values of 185.76 and 215.08

MPa. Of particular significance is the reversal in the relative YS of A356 and A356-0.4Sc. Although A356-0.4Sc exhibited a lower YS than the baseline alloy at ambient temperature, its YS became higher than that of baseline A356 following exposure and testing at 200 °C. This behaviour becomes clearer when the relative loss in YS is considered. The YS decreases by approximately 28.18% for the baseline A356 alloy between ambient temperature and 200 °C, compared with approximately 24.98% for A356-0.2Sc and 23.72% for A356-0.4Sc. Thus, A356-0.4Sc exhibits the smallest proportional reduction in YS despite having the lowest initial ambient-temperature YS. A356-0.2Sc, however, combines a high initial YS with improved strength retention and consequently maintains the highest absolute YS at 200 °C. These results suggest a distinction between the microstructural state that maximises ambient-temperature strength and that which provides resistance to strength degradation during elevated-temperature exposure. The enhanced strength retention is also accompanied by increased ductility, with elongation at 200 °C increasing from 12.21% for baseline A356 to 15.98% and 17.88% for the 0.2 and 0.4 wt.% Sc alloys, respectively.

In conventional T6-treated A356, an important contribution to strength originates from the fine Mg-Si-based precipitation structure within the α-Al matrix. In peak-aged Al-Si-Mg alloys, β″ is generally regarded as the major strengthening precipitate because its fine dimensions, high number density and close interparticle spacing provide effective resistance to dislocation motion. The precipitation sequence is nevertheless more complex than a simple β″ → β′ → β transformation, and intermediate structures including β′, U1, U2 and B′ may coexist during more advanced stages of precipitation. U1, for example, has been identified as a trigonal $MgAl_2Si_2$ metastable phase with crystallographic relationships to the α-Al matrix and other precipitate structures in the Al-Mg-Si system [49] .

The additional 60 min thermal exposure at 200 °C applied prior to tensile testing is expected to promote continued evolution of this metastable precipitation structure. Increasing temperature enhances atomic diffusivity, facilitating precipitate growth, transformation and coarsening. As the initially fine strengthening precipitates evolve towards coarser, later-stage Mg-Si-based structures, the effective precipitate number density decreases and interparticle spacing increases, progressively reducing their effectiveness as obstacles to dislocation motion. Studies of A356-related compositions aged at 200 °C demonstrate continued evolution of the precipitation structure with exposure time [50] .

Journal Pre-proof

The TEM observations provide a possible microstructural origin for this improved strength retention. HAADF-STEM examination of the A356-0.2Sc alloy in Figure 15 reveals an Al-Si-Sc-rich particle within the α-Al matrix. STEM-EDS mapping demonstrates pronounced co-enrichment of Sc and Si within the particle, while quantitative compositional analysis is consistent with the $AlSc_2Si_2$-type phase. Atomic-resolution HAADF-STEM imaging, together with the corresponding FFT indexed along the [001] zone axis and comparison with the simulated diffraction pattern, further confirms the ordered crystallographic structure of the Sc-containing particle.

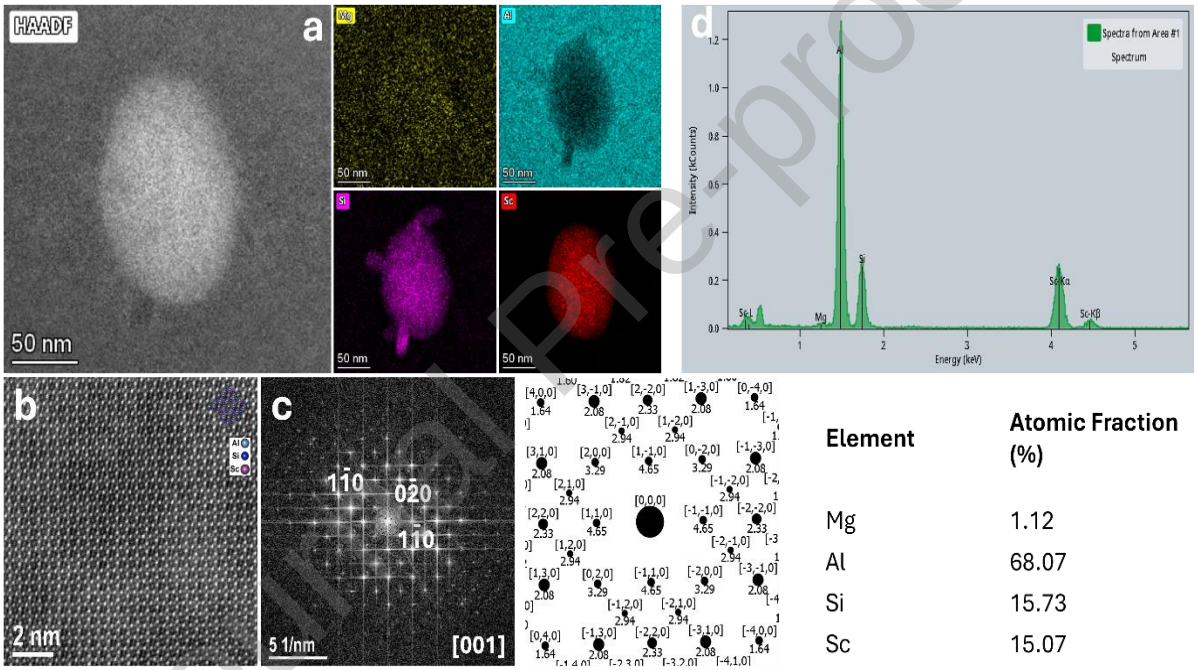


Figure 15. STEM characterisation of an Sc-containing particle in the T6-treated A356-0.2Sc alloy: (a) HAADF-STEM image showing an individual Al-Si-Sc-rich particle within the α-Al matrix and corresponding STEM-EDS elemental maps; (b) atomic-resolution HAADF-STEM image showing the ordered structure of the $AlSc_2Si_2$ phase; (c) corresponding FFT indexed along the [001] zone axis and simulated diffraction pattern for comparison; and (d) EDS spectrum obtained from the particle. The elemental distribution additionally indicates Mg enrichment in the vicinity of the particle/matrix interface.

More importantly, atomic-resolution examination of the $AlSc_2Si_2$/α-Al interfacial region in Figure 16 reveals the presence of an associated Mg-Si-based precipitate. The additional FFT

analysis demonstrates that this interfacial precipitate is crystallographically consistent with the metastable U1-$(AlSi)_2Mg$ phase. U1 is an established intermediate precipitate in the Al-Mg-Si system (both wrought and foundry alloys) and is structurally related to β′, U2 and other Mg-Si-based precipitate structures. Previous crystallographic studies report U1 as a trigonal $MgAl_2Si_2$ phase and demonstrate crystallographic coherency relationships with the α-Al matrix [49,51–53] .

The identification of U1 at the examined interface does not imply that all Mg-Si-based precipitates associated with $AlSc_2Si_2$ are necessarily U1. Depending on the local composition, thermal history and stage of precipitation evolution, different metastable and intermediate Mg-Si-based structures may potentially occur. Accordingly, the broader term Mg-Si-based precipitates is used here for associated precipitates whose crystallographic structures have not been individually established, while the term U1 is reserved for the precipitate directly identified through the atomic-resolution imaging and FFT analysis. The significance of the U1 observation is therefore that it provides direct evidence that Mg-Si-based precipitation occurs in close association with $AlSc_2Si_2$ and that the local precipitation environment adjacent to the Sc-containing dispersoid differs from that of the bulk α-Al matrix.

Journal Pre-proof

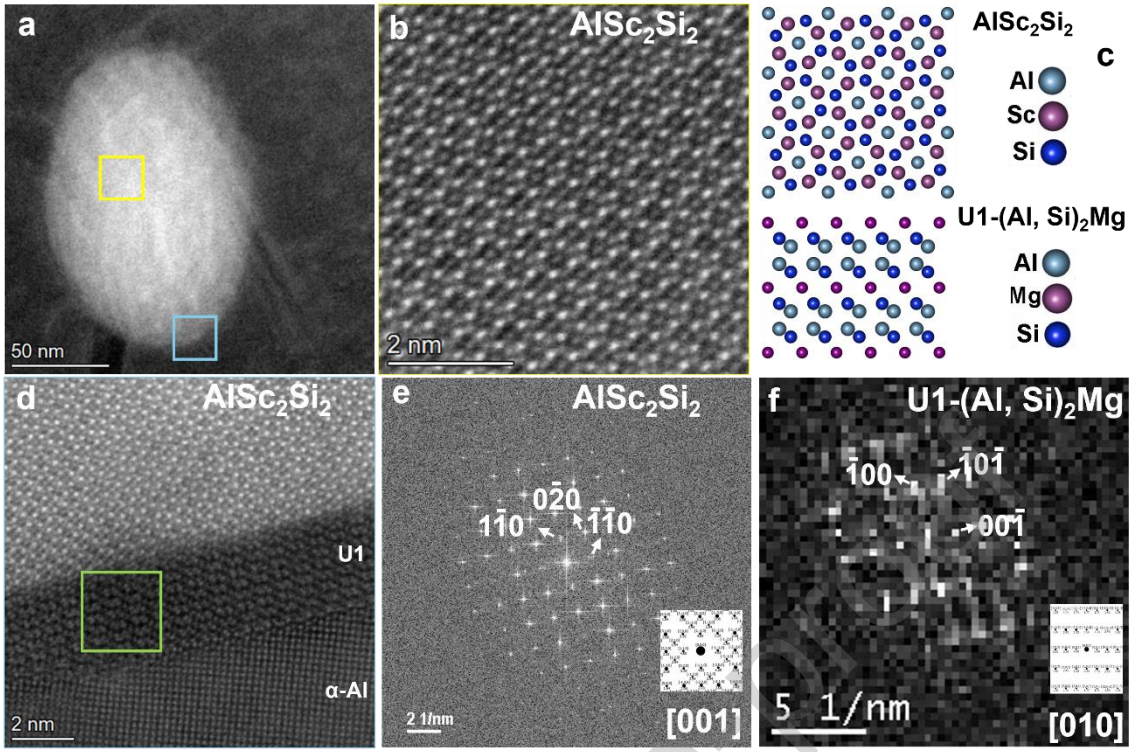


Figure 16. Microstructural and crystallographic characterization of the $AlSc_2Si_2$/α-Al interfacial region. (a) Low-magnification HAADF-STEM image showing a representative $AlSc_2Si_2$ dispersoid embedded within the α-Al matrix; the yellow square indicates the region selected for atomic-resolution imaging and the blue square marks the dispersoid/ matrix interface. (b) Atomic-resolution HAADF-STEM image of $AlSc_2Si_2$ viewed along the [001] zone axis (c) Projected atomic models of the $AlSc_2Si_2$ and U1-$(Al,Si)_2Mg$ phases. (d) Atomic-resolution HAADF-STEM image of the $AlSc_2Si_2$/α-Al interface, revealing an associated ordered Mg-Si-based phase; the green square indicates the region used for FFT analysis. (e) FFT obtained from the $AlSc_2Si_2$ region, indexed along the [001] zone axis; the inset shows the corresponding simulated electron diffraction pattern. (f) FFT obtained from the U1 region marked in (d), indexed along the [010] zone axis; the inset shows the corresponding simulated diffraction pattern, supporting the identification of the U1 phase.

This interpretation is further supported by the STEM-EDS results shown in Figure 17. Pronounced Mg enrichment occurs at the $AlSc_2Si_2$/α-Al interfacial region, accompanied by compositional variations in Si and Sc, while the Al distribution remains comparatively uniform. The spatial correspondence between Mg enrichment and the Mg-Si-based precipitation observed by atomic-resolution microscopy is consistent with local redistribution

of the principal age-hardening solutes towards the Sc-containing dispersoid. Taken together, the crystallographic and compositional observations demonstrate that $AlSc_2Si_2$ is not simply an isolated dispersoid within the α-Al matrix but is closely associated with the local Mg-Si precipitation environment.

Based on these observations, a possible local precipitation-stabilisation mechanism is proposed. In conventional peak-aged A356, the metastable Mg-Si-based precipitate population progressively evolves during exposure at 200 °C through transformation, growth and coarsening, reducing the effectiveness of the precipitation-strengthened microstructure. In the Sc-containing alloys, $AlSc_2Si_2$ dispersoids introduce chemically and crystallographically distinct interfaces into the α-Al matrix. The observed Mg enrichment and associated Mg-Si-based precipitation demonstrate that these interfaces may influence the local redistribution and precipitation behaviour of Mg and Si. The identification of U1 at one such interface provides direct crystallographic evidence for this altered local precipitation environment.

It is therefore proposed that the close association between $AlSc_2Si_2$ and Mg-Si-based precipitates may locally modify their thermally activated transformation and coarsening during short-term exposure at 200 °C. In this interpretation, $AlSc_2Si_2$ does not completely suppress the evolution of Mg-Si precipitates throughout the matrix. Instead, the comparatively stable dispersoid and its associated interface create local regions in which the precipitation pathway and solute redistribution are modified. The progression of the surrounding Mg-Si-based strengthening structure towards coarser and less effective precipitation states may consequently be delayed, allowing a greater fraction of the fine strengthening population to remain effective during elevated-temperature exposure.

Journal Pre-proof

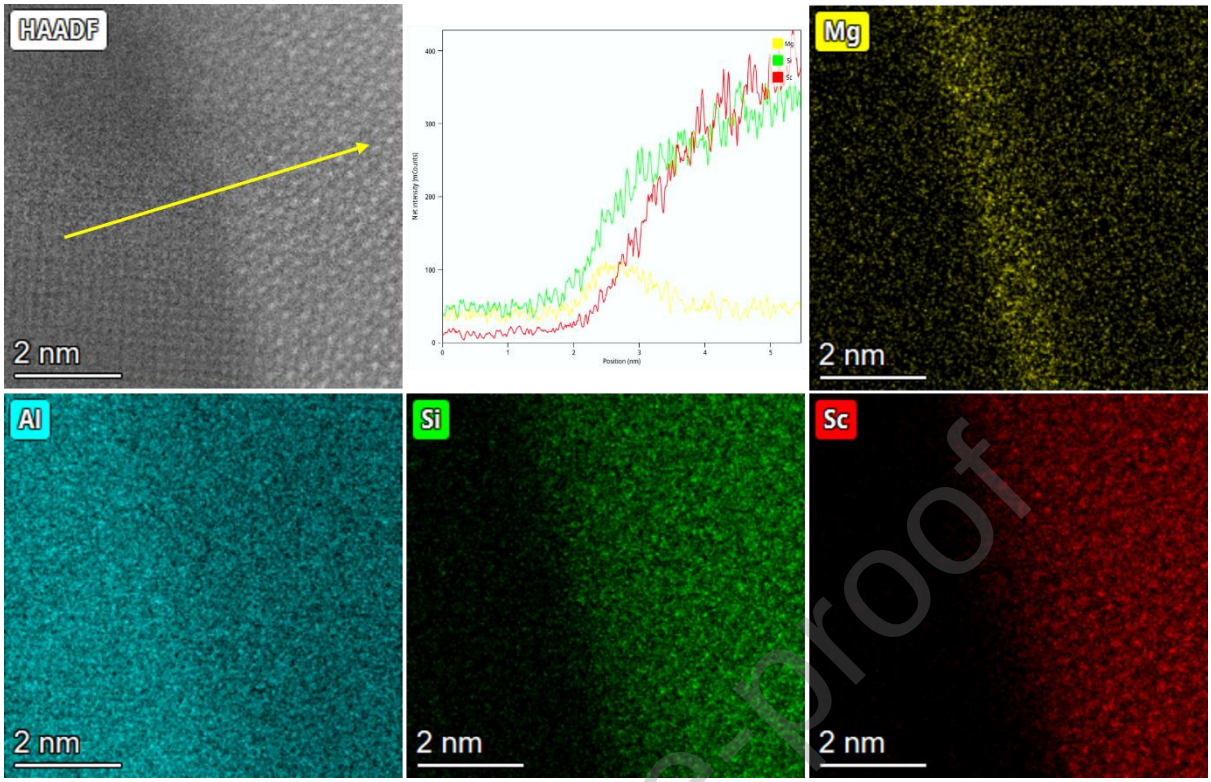


Figure 17. HAADF-STEM image, the intensity line profile (indicated by the yellow arrow) and corresponding STEM-EDS elemental maps acquired across the $AlSc_2Si_2$/α-Al interfacial region. The elemental distribution reveals pronounced Mg enrichment at the particle/matrix interface accompanied by compositional variations in Si and Sc. The local Mg enrichment coincides with the region in which interfacial Mg-Si-based precipitation is observed.

The proposed interpretation is consistent with previous observations in other transition-element-modified cast Al alloys. Zeng et al. [54] observed Mg segregation associated with the Al_2Si_2Ce/α-Al interface in an Al-Si-Mg-Ce alloy and discussed the role of interfacial effects in the stability and mechanical behaviour of the second phase. Although the intermetallic chemistry differs from the present $AlSc_2Si_2$ phase, this study provides a relevant Al-Si-Mg-based example in which interfacial solute segregation is associated with second-phase stability. Similarly, Yang et al. [55] demonstrated by atom probe tomography that Sc preferentially segregates to strengthening θ′-precipitate/matrix interfaces in Al-Cu alloys, where it lowers the interfacial energy and significantly suppresses precipitate coarsening during thermal exposure. More recently, Yan et al. [56] also showed that Sc-rich interfacial layers evolve into Al_3Sc/θ′/Al_3Sc multilayer composite precipitates that increase the energetic barrier for interface migration and substantially retard precipitate coarsening. Although these

studies were conducted on Al-Cu alloys strengthened by θ′ precipitates rather than β′-Mg_2Si, the underlying mechanism of interface stabilisation provides a relevant conceptual analogy to the present observations.

The present observations are also consistent with those reported by Rahimian et al. [57], who demonstrated that the addition of Zr to an Al-7Si alloy significantly improved tensile properties at 200 °C through the formation of coherent and semi-coherent Al-Si-Zr-Ti precipitates, which remained stable because of the extremely low diffusivity of Zr in α-Al. These precipitates resisted Ostwald ripening and continued to impede dislocation motion after the conventional strengthening precipitates had begun to coarsen, resulting in superior strength retention compared with the base alloy. Ding et al. [58] reported that Sc-modified A356 alloys retained excellent thermal stability following prolonged exposure at 200 °C and attributed this behaviour to the combined effects of refined SDAS, spheroidized eutectic Si and thermally stable Sc-containing precipitates. Based on these findings, they proposed Sc-modified A356 alloys as promising materials for elevated-temperature applications. However, their study evaluated room-temperature tensile properties after thermal exposure rather than tensile behaviour directly at elevated temperature.

Taken together, these observations suggest that the combination of direct strengthening from the Sc-containing dispersoids and improved local retention of Mg-Si-based precipitation provides a plausible explanation for the higher strength retained by the Sc-modified alloys at 200 °C. It should nevertheless be emphasised that the present microscopy directly demonstrates the formation of $AlSc_2Si_2$, the spatial association of Mg-Si-based precipitation with $AlSc_2Si_2$, local Mg enrichment at the particle/matrix interface and the crystallographic identification of U1 phase at the atomic-resolution-characterised interface. The proposed retardation of Mg-Si precipitate transformation and coarsening is inferred from these observations and the corresponding improvement in elevated-temperature strength retention rather than being directly measured. Quantitative measurements of the size, number density and phase constitution of Mg-Si-based precipitates before and after controlled thermal exposures would be required to establish the transformation and coarsening kinetics directly. Nevertheless, the combination of the tensile results and atomic-scale observations along with the relevant literature studies provides a consistent basis for proposing that Sc addition

contributes not only through direct dispersoid strengthening, but also through modification of the local thermal stability of the Mg-Si precipitation-strengthened microstructure.

4.4 Microstructure-Controlled Fatigue Behaviour

Figure 7 presents the S-N curves of the baseline A356-T6 and Sc-modified A356-0.2Sc-T6 alloys. The A356-0.2Sc-T6 alloy exhibited higher fatigue lives at several of the investigated stress amplitudes compared with the baseline alloy, although some scatter is observed, which is typical for cast Al-Si alloys owing to the distribution of casting defects. Fatigue behaviour in cast Al-Si alloys is strongly influenced by local microstructural heterogeneities and casting-related defects, including porosity, oxide-related defects, coarse eutectic Si and Fe-rich intermetallic particles, which can act as local stress concentrators and preferential sites for fatigue crack initiation [2,59]. Consequently, the refinement of these features delays crack initiation by promoting a more homogeneous stress distribution and reducing localised plastic deformation. The better fatigue behaviour arises from the combination of refined microstructure during solidification, reduced casting defects and precipitate strengthening after T6 heat treatment [1,2,60].

As discussed previously, the addition of 0.2 wt.% Sc significantly refined the grain structure from 540 μm to 338 μm, reduced the secondary dendrite arm spacing (SDAS) from 24 μm to 22 μm and modified the eutectic Si from coarse acicular to a finer fibrous morphology. These solidification-induced microstructural features are largely retained and continue to play a critical role in fatigue performance post T6 heat treatment as well. Another important aspect is the morphology of Fe intermetallic, particularly the needle-like β-Al_5FeSi intermetallic as shown in Figure 18d which remains undissolved even after heat treatment. Numerous studies have shown how these particles act as stress concentrators and reduce the fatigue performance of the alloy [59,61]. It is therefore important to modify the morphology of these intermetallics to improve the fatigue life. SEM observations (Figure 18c) together with STEM-EDS analysis (Figure 18a and Figure 18b) demonstrates that Sc modifies the conventional acicular β-Al_5FeSi phase into compact nodular Al_5Fe(Si, Sc) and π-$Al_8Mg_3Si_6Fe$ to Sc containing Al-Fe-Mg-Si intermetallics. Compared with the long needle-like β-Al_5FeSi intermetallics present in the baseline alloy, these nodular particles exhibit a much lower aspect ratio and therefore generate considerably lower local stress concentrations. Consequently, the tendency for crack nucleation at Fe-bearing intermetallics

is significantly reduced, contributing to the improved fatigue crack initiation resistance of the Sc-modified alloy.

In addition to these microstructural changes, quantitative image analysis was performed to examine differences in the casting-related defect population. As shown in Figure 10 and Table 3, the measured area fraction of porosities decreased from 0.51 ± 0.09% for A356 to 0.35 ± 0.03% for A356-0.2Sc. The mean Feret diameter decreased from 113.90 ± 21.77 μm to 101.37 ± 25.83 μm, while the maximum Feret diameter decreased from 286.43 μm to 202.72 μm. These results indicate that Sc addition reduced the measured defect area fraction and characteristic defect dimensions under the non-degassed casting conditions investigated. Although the defect analysis was performed on samples that were not used for fatigue testing, the observed reduction in defect population suggests a potential beneficial influence of Sc addition on casting quality. Since casting defects, particularly larger pores, can act as preferential sites for fatigue crack initiation, this reduction may also contribute to the improved fatigue performance observed in the Sc-containing alloy. However, this possible contribution should be interpreted with caution, as the porosity measurements were not directly characterised in the fatigue-tested specimens. The fatigue behaviour discussed above is based on the degassed and T6-treated specimens. Similar observations were made by Limmaneevichitr et al. [62], who reported that the addition of 0.2 wt.% Sc to Al-Si-Mg alloys reduced the total porosity area and redistributed porosity into finer and more uniformly dispersed defects through a change in eutectic solidification mode. They further demonstrated that Sc simultaneously refines the grain structure and modifies the eutectic Si morphology, resulting in fewer large shrinkage cavities and a lower porosity concentration in the hot-spot region. Since fatigue life in cast aluminium alloys is governed predominantly by the largest casting defect rather than the average porosity level, the reduction in pore size and the elimination of large, interconnected shrinkage defects substantially delay fatigue crack initiation. However, the same study also showed that increasing the Sc content promoted the formation of coarse $AlSc_2Si_2$ particles, which increased oxidation and hindered liquid feeding during solidification, thereby increasing overall porosity. These observations support the present selection of 0.2 wt.% Sc, where sufficient Sc is available to maximise grain refinement while avoiding excessive porosity associated with higher Sc additions.

After T6 heat treatment, precipitation strengthening may provide an additional contribution to the fatigue response. The present TEM observations identified ordered $AlSc_2Si_2$ particles in close spatial association with Mg-Si-based precipitation and localised Mg enrichment, with

U1-$MgAl_2Si_2$ specifically identified at one atomic-resolution-characterised interface. Such features may influence cyclic dislocation motion and local plastic deformation by providing multiple obstacles to cyclic dislocation motion. Consequently, the localisation of cyclic plastic strain might be reduced, delaying persistent slip band formation and improving resistance to fatigue crack initiation. However, the present study did not systematically quantify precipitate evolution during cyclic loading or thermal exposure, and therefore the specific contribution of $AlSc_2Si_2$ precipitate to fatigue resistance cannot be established directly from the present observations.

The fatigue strengthening mechanism proposed in the present study is consistent with previous investigations on rare-earth-modified cast aluminium alloys. Liu et al. [60] reported that Zr addition significantly improved the high-cycle fatigue performance and elevated-temperature mechanical properties of Al-Si-Cu-Mg alloys through the combined effects of grain refinement, reduced secondary dendrite arm spacing (SDAS), lower porosity, and precipitation strengthening by thermally stable Al-Si-Zr-Ti precipitates. Similarly, Masita et al. [63] demonstrated that the addition of 0.4 wt.% Sc enhanced the fatigue properties of A356 alloy after T6 heat treatment, which they primarily attributed to the higher tensile strength achieved through Sc addition.

Overall, the fatigue response of the A356-0.2Sc-T6 alloy appears to result from the combined influence of grain refinement, reduced SDAS, eutectic Si modification, changes in Fe-bearing intermetallic morphology, differences in the measured porosities and precipitation strengthening after T6 treatment. These factors may act together to modify local stress concentrations and cyclic plastic deformation, thereby influencing fatigue crack initiation and propagation.

Journal Pre-proof

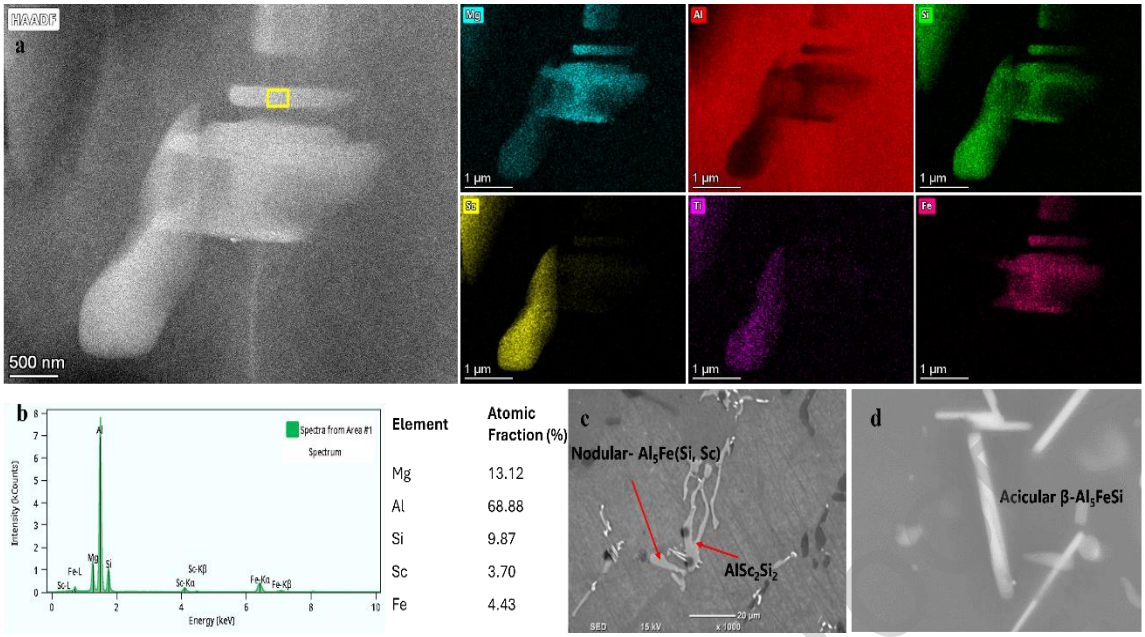


Figure 18. STEM characterisation of the Fe-based intermetallic with: (a) HAADF-STEM image of the Sc-modified Fe-bearing phase with the corresponding STEM-EDS elemental maps; (b) corresponding EDS analysis from the highlighted yellow box; (c) SEM image of the Sc-modified nodular Fe-intermetallic from the A356-0.2Sc alloy; and (d) SEM image of the unmodified acicular Fe-intermetallic from the baseline A356 alloy.

5. Conclusions

The effect of Sc addition on the microstructure, fluidity, fading resistance, elevated-temperature tensile properties and fatigue performance of A356.2 alloy was systematically investigated. The following conclusions can be drawn:

1. The addition of 0.2 wt.% Sc significantly refined the grain structure, reduced SDAS, modified eutectic Si and transformed acicular β-Al_5FeSi intermetallics into compact Sc-containing Fe-rich phases, resulting in a more homogeneous microstructure.
2. An optimum Sc addition of 0.2 wt.% increased the fluidity by 19.5% compared with the baseline alloy. Further increases in Sc content reduced fluidity due to the formation of coarse primary Sc-containing intermetallics.
3. The Sc-modified alloy maintained relatively stable grain size during prolonged melt holding under the present experimental conditions, with an approximately 14% increase in grain size between 30 and 240 min. These results demonstrate good retention of Sc-induced grain-refining effectiveness during prolonged melt holding.

4. After T6 treatment, the Sc-modified alloys exhibited improved tensile-strength retention and higher ductility at 200 °C compared with the baseline alloy. Atomic-resolution characterisation revealed Mg-Si-based precipitation associated with $AlSc_2Si_2$ dispersoids, with U1-$MgAl_2Si_2$ specifically identified at an examined $AlSc_2Si_2$/α-Al interface together with localised Mg enrichment. These observations suggest that the Sc-containing dispersoids modify the local Mg-Si precipitation environment and may contribute to improved retention of precipitation strengthening during elevated-temperature exposure.

5. The Sc-modified alloy also showed improved fatigue performance at several of the investigated stress amplitudes, attributed to the synergistic effects of grain refinement & SDAS reduction, reduced casting defects, modified Fe-rich intermetallics and the additional strengthening from Al-Si-Sc particles, which may contribute to delaying fatigue crack initiation and propagation.

Declaration of competing interests

The authors declare that they have no conflict of interest.

Acknowledgements

This research was funded by the Engineering and Physical Sciences Research Council (EPSRC) under project UKRI1682 and Innovate UK (IUK) under grant number APC 10113213. Priyansh Khandelwal would like to acknowledge Niocorp Developments Limited, USA, for their support. The authors would like to acknowledge the use of the BCAST Advanced Characterisation Suite (BACS) set up through the funding received from the UKRI Infrastructure grant entitled “Future Metallurgy Centre”

Data Availability Statement

Data will be made available on request.

Journal Pre-proof

Rights retention statement

For the purposes of open access, the author has applied a Creative Commons Attribution (CC BY) Licence to any Accepted Author Manuscript version arising from this submission.

References

1. Dash SS., Chen D. A Review on Processing–Microstructure–Property Relationships of Al-Si Alloys: Recent Advances in Deformation Behavior. Metals. MDPI; 2023. Available at: DOI:10.3390/met13030609

2. Wang QG., Apelian D., Lados DA. Fatigue behavior of A356-T6 aluminum cast alloys. Part I. E□ect of casting defects. Available at: www.elsevier.com/locate/ligandmet

3. Javidani M., Larouche D. Application of cast Al-Si alloys in internal combustion engine components. International Materials Reviews. 2014. pp. 132–158. Available at: DOI:10.1179/1743280413Y.0000000027

4. Khandelwal P., Huang Y., Nunn J., Honan S., Ji S. Effect of Scandium Addition on the Microstructure and Mechanical Properties of Al–7Si–0.3Mg Cast Alloy. 2026. pp. 1419–1427. Available at: DOI:10.1007/978-3-032-13832-3_185

5. Khandelwal P., Negrea RF., Nunn J., Honan S., Ji S. Optimum scandium addition in A356 cast alloys: alloy design, microstructural evolution and mechanical properties. Materials & Design. June 2026; 266: 116184. Available at: DOI:10.1016/j.matdes.2026.116184

6. Ravi KR., Pillai RM., Amaranathan KR., Pai BC., Chakraborty M. Fluidity of aluminum alloys and composites: A review. Journal of Alloys and Compounds. 2008. pp. 201–210. Available at: DOI:10.1016/j.jallcom.2007.02.038

7. Samuel E., Samuel AM., Songmene V., Samuel FH. A Review on the Analysis of Thermal and Thermodynamic Aspects of Grain Refinement of Aluminum-Silicon-Based Alloys. Materials. Multidisciplinary Digital Publishing Institute (MDPI); 2023. Available at: DOI:10.3390/ma16165639

8. Mohanty PS., Gruzleskit JE. MECHANISM OF GRAIN REFINEMENT IN ALUMINIUM. ~ Pergamon Acta metall..tater. 2001.

9. Limmaneevichitr C., Eidhed W. Fading mechanism of grain refinement of aluminum-silicon alloy with Al-Ti-B grain refiners. Materials Science and Engineering: A. Elsevier BV; 25 May 2003; 349(1–2): 197–206. Available at: DOI:10.1016/S0921-5093(02)00751-7

10. Schaffer PL., Dahle AK. Settling behaviour of different grain refiners in aluminium. Materials Science and Engineering: A. Elsevier BV; 15 December 2005; 413–414: 373–378. Available at: DOI:10.1016/j.msea.2005.08.202

11. Oh B. The Exponential Law of Endurance Tests. American Society for Testing and Materials. 1910. pp. 625–630.

12. Ravi KR., Pillai RM., Amaranathan KR., Pai BC., Chakraborty M. Fluidity of aluminum alloys and composites: A review. Journal of Alloys and Compounds. 2008. pp. 201–210. Available at: DOI:10.1016/j.jallcom.2007.02.038

13. Mollard FR., Flemings MC., Niyama EF. Aluminum Fluidity in Casting. JOM. 26 November 1987; 39(11): 34–34. Available at: DOI:10.1007/BF03257537

14. Tiryakioglu M., Askeland DR., Ramsay C. The Fluidity of 319 and A356: An Experimental Design Approach. Transactions-American Foundrymens Society. 1994; 102: 17–25.

15. Dahle AK., Tøndel PA., Paradies CJ., Arnberg L. Effect of grain refinement on the fluidity of two commercial Al-Si foundry alloys. Metallurgical and Materials Transactions A. August 1996; 27(8): 2305–2313. Available at: DOI:10.1007/BF02651885

16. Kwon YD., Lee ZH. The effect of grain refining and oxide inclusion on the fluidity of Al-4.5Cu-0.6Mn and A356 alloys. Materials Science and Engineering: A. Elsevier BV; 15 November 2003; 360(1–2): 372–376. Available at: DOI:10.1016/S0921-5093(03)00504-5

17. Bäckerud Lennart., Chai Guocai., Tamminen Jarmo. Solidification characteristics of aluminium alloys. Vol 2, Foundry alloys. Skanaluminium; 1990. 255 p.

18. Arnberg L., Chai G., Backerud L. Determination of dendritic coherency in solidifying melts by rheological measurements. Materials Science and Engineering: A. December 1993; 173(1–2): 101–103. Available at: DOI:10.1016/0921-5093(93)90195-K

19. Malekan M., Shabestari SG. Effect of grain refinement on the dendrite coherency point during solidification of the A319 aluminum alloy. Metallurgical and Materials Transactions A: Physical Metallurgy and Materials Science. December 2009; 40(13): 3196–3203. Available at: DOI:10.1007/s11661-009-9978-y

20. Yang L., Li W., Du J., Wang K., Tang P. Effect of Si and Ni contents on the fluidity of Al-Ni-Si alloys evaluated by using thermal analysis. Thermochimica Acta. Elsevier B.V.; 10 December 2016; 645: 7–15. Available at: DOI:10.1016/j.tca.2016.10.013

21. Wu D., Wang Y., Li F., Xue Y., Li J., Su R. Controlling eutectic Si in Al–Si casting alloys: From fundamental mechanisms to performance. Journal of Materials Research and Technology. Elsevier Editora Ltda; 1 March 2026; 41: 7741–7778. Available at: DOI:10.1016/j.jmrt.2026.03.013

22. Timpel M., Wanderka N., Schlesiger R., Yamamoto T., Lazarev N., Isheim D., et al. The role of strontium in modifying aluminium-silicon alloys. Acta Materialia. May 2012; 60(9): 3920–3928. Available at: DOI:10.1016/j.actamat.2012.03.031

23. Kotte B. Strontium modification gives critical melt control. Metal Casting. 1985; 75(5): 31–33.

24. Seshadri MR., Ramachandran A. Fluidity of Modified Aluminum-Silicon Alloys. Modern Castings. 1965; 21: 110–122.

Journal Pre-proof

25. Di Sabatino M., Shankar S., Apelian D. Shape casting: The John Campbell symposium. The Minerals, Metals & Materials Society. . 2005. pp. 193–202.

26. Çolak M., Kayikci R., Dispinar D. Influence of Different Cross Sections on Fluidity Characteristics of A356. Transactions of the Indian Institute of Metals. Springer; 1 April 2015; 68(2): 275–281. Available at: DOI:10.1007/s12666-014-0455-y

27. Dahle AK., Arnberg L., Apelian D. Burst Feeding and Its Role in Porosity Formation During Solidification of Al Foundry Alloys. Transactions of the American Foundrymen's Society. 1997; 105: 963–970.

28. Taghaddos E., Hejazi MM., Taghiabadi R., Shabestari SG. Effect of iron-intermetallics on the fluidity of 413 aluminum alloy. Journal of Alloys and Compounds. 22 January 2009; 468(1–2): 539–545. Available at: DOI:10.1016/j.jallcom.2008.01.079

29. Chanyathunyaroj K., Patakham U., Kou S., Limmaneevichitr C. Microstructural evolution of iron-rich intermetallic compounds in scandium modified Al-7Si-0.3Mg alloys. Journal of Alloys and Compounds. Elsevier B.V; 2017; 692: 865–875. Available at: DOI:10.1016/j.jallcom.2016.09.132

30. Tzeng YC., Wu CT., Bor HY., Horng JL., Tsai ML., Lee SL. Effects of scandium addition on iron-bearing phases and tensile properties of Al-7Si-0.6Mg alloys. Materials Science and Engineering: A. Elsevier; 2014; 593: 103–110. Available at: DOI:10.1016/j.msea.2013.11.039

31. Patakham U., Limmaneevichitr C. Effects of iron on intermetallic compound formation in scandium modified Al-Si-Mg Alloys. Journal of Alloys and Compounds. Elsevier Ltd; 15 December 2014; 616: 198–207. Available at: DOI:10.1016/j.jallcom.2014.07.037

32. Niu G., Mao J., Wang J. Effect of Ce Addition on Fluidity of Casting Aluminum Alloy A356. Metallurgical and Materials Transactions A: Physical Metallurgy and Materials Science. Springer Boston; 1 December 2019; 50(12): 5935–5944. Available at: DOI:10.1007/s11661-019-05458-9

33. Puparattanapong K., Pandee P., Boontein S., Limmaneevichitr C. Fluidity and Hot Cracking Susceptibility of A356 Alloys with Sc Additions. Transactions of the Indian Institute of Metals. Springer India; 1 July 2018; 71(7): 1583–1593. Available at: DOI:10.1007/s12666-018-1293-0

34. Prukkanon W., Srisukhumbowornchai N., Limmaneevichitr C. Influence of Sc modification on the fluidity of an A356 aluminum alloy. Journal of Alloys and Compounds. 2009; 487(1–2): 453–457. Available at: DOI:10.1016/j.jallcom.2009.07.169

35. Mao G., Wu Z., Liu S., Zhong L., Gao W. The fluidity of A357 alloy with scandium (Sc) and zirconium (Zr) addition. Journal of Materials Research and Technology. Elsevier Editora Ltda; 1 November 2020; 9(6): 13570–13574. Available at: DOI:10.1016/j.jmrt.2020.09.111

Journal Pre-proof

36. Murty BS., Kori SA., Chakraborty M. Grain refinement of aluminium and its alloys by heterogeneous nucleation and alloying. International Materials Reviews. 18 February 2002; 47(1): 3–29. Available at: DOI:10.1179/095066001225001049

37. Wang Y., Que Z., Hashimoto T., Zhou X., Fan Z. Mechanism for Si Poisoning of Al-Ti-B Grain Refiners in Al Alloys. Metallurgical and Materials Transactions A: Physical Metallurgy and Materials Science. Springer; 1 November 2020; 51(11): 5743–5757. Available at: DOI:10.1007/s11661-020-05950-7

38. Qiu D., Taylor JA., Zhang MX., Kelly PM. A mechanism for the poisoning effect of silicon on the grain refinement of Al-Si alloys. Acta Materialia. February 2007; 55(4): 1447–1456. Available at: DOI:10.1016/j.actamat.2006.09.046

39. Silva EL., Kultz Unti LF., V. Tosetti JP., Antunes AS., Zilnyk K. Grain refining and fading mechanisms in a eutectic Al-Si alloy refined with Al-Nb-B. Journal of Alloys and Compounds. Elsevier Ltd; 15 October 2025; 1042. Available at: DOI:10.1016/j.jallcom.2025.183914

40. Zhou Y., Xu Y., Xiang Y., Chen G., Ni X., Liu L., et al. Grain Refining Efficiency of Al-V-B Master Alloy in A356.2 Alloy Under Different Inoculated Temperatures and Holding Times. JOM. Springer; 1 December 2024; 76(12): 6962–6971. Available at: DOI:10.1007/s11837-024-06632-0

41. Ran Q., Hu M., Liu T., Wang F., Jiang B., Xu H., et al. Evolution of (Ti, V) Compounds in the Al-Ti-V-B System and the Refinement Performance Thereof. JOM. Springer; 1 January 2025; 77(1): 261–270. Available at: DOI:10.1007/s11837-024-06981-w

42. Ding W., Li C., Chen T., Zhao W., Guo T., Qiao J., et al. Grain Refinement of Al-5Ti-0.62C-0.2Nd Grain Refiner for Commercial Pure Aluminum and Its Effect on Mechanical Properties. Materials Research. 3 December 2018; 22(1). Available at: DOI:10.1590/1980-5373-mr-2018-0302

43. Muangnoy P., Eidhed K. Fading mechanism on grain refinement and modification with Al-B-Sr master alloys in an aluminium-silicon cast alloy. Archives of Metallurgy and Materials. Polska Akademia Nauk; 2022; 67(3): 1137–1144. Available at: DOI:10.24425/amm.2022.139713

44. Eidhed K., Muangnoy P. Grain refinement and eutectic modification of A356 casting alloy by adding Al-B-Sr master alloys and its effect on tensile properties. Materials Research Express. Institute of Physics; 1 October 2022; 9(10). Available at: DOI:10.1088/2053-1591/ac99c1

45. Selling BI. A Casting defects and the tensile properties of an A1-Si-Mg alloy. 1996.

46. Lian P., Mao H., Wei Q., Ma R., Li C., Xu H. The formation of (Al, Si)3(Ti, Sc) through microalloying and solidification control synergy in Al-7Si-0.7Mg refines α-Al greatly. Journal of Alloys and Compounds. Elsevier B.V.; 2023; 967(June): 171741. Available at: DOI:10.1016/j.jallcom.2023.171741

47. Mao H., Lian P., Wei Q., Wang Y., Xu H., Li Y. Effect of scandium on grain refinement mechanism and mechanical properties of Al–7Si–0.6 Mg alloy at different cooling

rates. Journal of Materials Research and Technology. The Author(s); 2023; 26: 4784–4796. Available at: DOI:10.1016/j.jmrt.2023.08.227

48. Pramod SL., Prasada Rao AK., Murty BS., Bakshi SR. Effect of Sc addition on the microstructure and wear properties of A356 alloy and A356-TiB2 in situ composite. Materials and Design. Elsevier Ltd; 2015; 78: 85–94. Available at: DOI:10.1016/j.matdes.2015.04.026

49. Andersen SJ., Marioara CD., Vissers R., Frøseth A., Zandbergen HW. The structural relation between precipitates in Al-Mg-Si alloys, the Al-matrix and diamond silicon, with emphasis on the trigonal phase U1-MgAl2Si2. Materials Science and Engineering: A. Elsevier BV; 25 January 2007; 444(1–2): 157–169. Available at: DOI:10.1016/j.msea.2006.08.084

50. Assadiki A., Esin VA., Martinez R., Poole WJ., Cailletaud G. Modelling precipitation hardening in an A356+0.5wt.%Cu cast aluminum alloy. 2021.

51. Dybowski B., Adamczyk-Cieślak B., Rodak K., Bednarczyk I., Kiełbus A., Mizera J. The Microstructure of AlSi7Mg Alloy in as Cast Condition. Solid State Phenomena. April 2015; 229: 3–10. Available at: DOI:10.4028/www.scientific.net/SSP.229.3

52. Ding L., Weng Y., Jia Z., Zang R., Xiang K., Liu Q., et al. Interactive transformation mechanisms of multiple metastable precipitates in a Si-rich Al-Mg-Si alloy. Philosophical Magazine. Taylor and Francis Ltd.; 2022; 102(16): 1602–1627. Available at: DOI:10.1080/14786435.2022.2051633

53. Faregh SM., Larouche D., Chen XG. Atomic scale characterization of precipitates in an Al-Si-Mg alloy containing excess Si and trace amounts of Cu. Materialia. Elsevier B.V.; 1 May 2025; 40. Available at: DOI:10.1016/j.mtla.2025.102396

54. Zeng L., Jin Y., Gao J., Yi W., Chen L., Zhang L. Achieving simultaneous improvement in strength and ductility in Al–Si–Mg–Ce alloy through synergistic morphology modification of eutectic (Si) and Al2Si2Ce phases by Sr addition. Journal of Materials Research and Technology. Elsevier Editora Ltda; 1 November 2024; 33: 975–981. Available at: DOI:10.1016/j.jmrt.2024.09.108

55. Yang C., Zhang P., Shao D., Wang RH., Cao LF., Zhang JY., et al. The influence of Sc solute partitioning on the microalloying effect and mechanical properties of Al-Cu alloys with minor Sc addition. Acta Materialia. Elsevier Ltd; 15 October 2016; 119: 68–79. Available at: DOI:10.1016/j.actamat.2016.08.013

56. Yan J., Dong L., Ming WQ., Gao YW., Zhao XQ., Wu CL., et al. Thermally stabilized interface structure of the θ′-precipitates in heat-resistant AlCu(ScZr) alloys. Journal of Alloys and Compounds. Elsevier Ltd; 15 May 2025; 1028. Available at: DOI:10.1016/j.jallcom.2025.180662

57. Rahimian M., Amirkhanlou S., Blake P., Ji S. Nanoscale Zr-containing precipitates; a solution for significant improvement of high-temperature strength in Al-Si-Cu-Mg alloys. Materials Science and Engineering: A. Elsevier Ltd; 4 April 2018; 721: 328–338. Available at: DOI:10.1016/j.msea.2018.02.060

Journal Pre-proof

58. Ding J., Zhang P., Li X., Wang L., Liao W., Huang L., et al. Microstructure and thermal stability evolution behavior of Sc-containing A356.2 aluminum alloy under cyclic thermal exposure conditions. Materials Science and Engineering: A. Elsevier Ltd; 18 April 2018; 723: 165–173. Available at: DOI:10.1016/j.msea.2018.03.002

59. Yi JZ., Gao YX., Lee PD., Lindley TC. Effect of Fe-content on fatigue crack initiation and propagation in a cast aluminum-silicon alloy (A356-T6). Materials Science and Engineering: A. Elsevier BV; 25 November 2004; 386(1–2): 396–407. Available at: DOI:10.1016/j.msea.2004.07.044

60. Liu G., Blake P., Ji S. Effect of Zr on the high cycle fatigue and mechanical properties of Al–Si–Cu–Mg alloys at elevated temperatures. Journal of Alloys and Compounds. Elsevier Ltd; 15 November 2019; 809. Available at: DOI:10.1016/j.jallcom.2019.151795

61. Kuchariková L., Medvecká D., Tillová E., Belan J., Kritikos M., Chalupová M., et al. The effect of the β-al5fesi phases on microstructure, mechanical and fatigue properties in a356.0 cast alloys with higher fe content without additional alloying of mn. Materials. MDPI AG; 2 April 2021; 14(8). Available at: DOI:10.3390/ma14081943

62. Puparattanapong K., Limmaneevichitr C. Effect of Scandium on Porosity formation in Al–6Si–0.3 Mg Alloys. Transactions of the Indian Institute of Metals. Springer India; 1 October 2016; 69(8): 1587–1594. Available at: DOI:10.1007/s12666-015-0732-4

63. Masita A., Yeo WH., Saw LH., Lim YP., Lee JW., Ng TC. Mechanical and Fatigue Properties of Gravity Die-Cast A356 Aluminium Alloy with Addition of Scandium. IOP Conference Series: Earth and Environmental Science. Institute of Physics Publishing; 2019. Available at: DOI:10.1088/1755-1315/268/1/012059

Journal Pre-proof

Declaration of Interest Statement

The authors declare that they have no known competing financial interests or personal relationships that could have appeared to influence the work reported in this paper.

Highlights

- 0.2 wt.% Sc increased A356 alloy fluidity by 19.5% via grain refinement.
- Sc showed excellent grain refinement stability after 240 min melt holding.
- Sc-containing A356 alloys showed improved tensile performance at 200 °C.
- HAADF-STEM revealed ordered $AlSi_2Sc_2$ and Mg-Si-based precipitates in close spatial relation.
- Sc enhanced fatigue properties through multiscale microstructural refinement.

Journal Pre-proof